We are IntechOpen,
the world's leading publisher of
Open Access books
Built by scientists, for scientists

4,800
Open access books available

122,000
International authors and editors

135M
Downloads

Our authors are among the

154
Countries delivered to

TOP 1%
most cited scientists

12.2%
Contributors from top 500 universities

CLARIVATE ANALYTICS

BOOK CITATION INDEX

INDEXED

WEB OF SCIENCE™

Selection of our books indexed in the Book Citation Index
in Web of Science™ Core Collection (BKCI)

Interested in publishing with us?
Contact book.department@intechopen.com

Detection of Magnetic Transitions by Means of Ferromagnetic Resonance and Microwave Absorption Techniques

H. Montiel and G. Alvarez

Additional information is available at the end of the chapter

http://dx.doi.org/10.5772/55962

1. Introduction

Due to nature of the magnetic materials, the experimental techniques to study their physical properties are generally sophisticated and expensive; and several techniques are used to obtain reliable information on the magnetic properties of these materials. One of the most employed techniques to characterize the magnetic materials is the electron magnetic resonance (EMR), also well-known as the ferromagnetic resonance (FMR) at temperatures below Curie temperature (T_c) and the electron paramagnetic resonance at temperatures above T_c. EMR is a powerful technique for studying the spin structure and magnetic properties in bulk samples, thin films and nanoparticles, being mainly characterized by means of two parameters: the resonant field (H_{res}) and the linewidth (ΔH_{PP}); these parameters reveal vital information on magnetic nature of the materials (Montiel et al., 2004, 2006; Alvarez et al., 2008, 2010). It is also necessary to mention that EMR is one of the most commonly used techniques to research the dependence of the magnetic anisotropy with respect to orientation of the sample (Montiel et al., 2007, 2008; G. Alvarez et al., 2008) and the temperature (Montiel et al., 2004; Alvarez et al., 2010); this technique is also applied to study magnetic relaxation in solid materials through their linewidth, and that it is due to conduction mechanisms and intrinsic relaxation.

In particular, EMR technique is employed with success to determine the onset of magnetic transitions (Okamura, 1951; Okamura et al., 1951; Healy, 1952; Montiel et al., 2004; Alvarez et al., 2006, 2010), such as the Néel transition (from a paramagnetic phase to antiferromagnetic ordering) and the Curie transition (from a ferromagnetic or ferrimagnetic order to paramagnetic phase); through changes in the spectral parameters. EMR around critical temperatures have been object of an active research, e.g. Okamura et al. (1951) have

studied the Néel transition in some materials by means of EMR technique. Fig. 1 shows the direct resonance absorption versus magnetic field for MnS in the 78-329 K temperature range. The height of the resonant absorption decreases and the linewidth is become broader with decreasing temperature, especially below the Néel temperature (T_N= 160 K); where the position of the maximum is found at a constant magnetic field of 3510 G for all the temperatures, suggesting the existence of a strong local magnetic field in this material.

The previous behavior is quite contrary to those of the ferromagnetic and ferrimagnetic materials around Curie transition. For example, Healy (1952) has employed EMR technique to study the nickel ferrite ($NiFe_2O_4$) in temperature range of 78 K to 861 K. In Fig. 2, the direct resonance spectra show that the linewidth decreases and a shift in resonant field were observed with increasing temperature, all these changes can be completely associated with the Curie transition (T_c= 858 K).

Okamura (1951) also carries out a characterization in the ferrite $NiFe_2O_4$ by means of EMR technique but at low temperature. Fig. 3 shows the direct resonance absorption with varying applied dc magnetic field at various temperatures in a disk $NiFe_2O_4$. In these spectra a double absorption were clearly observed, and both absorptions are dependent of the temperature; where one of the absorptions is near to zero magnetic field. In our EMR measurements, we also detected a second absorption mode around zero field in amorphous alloys (Montiel et al., 2005) and ferrites (Montiel et al., 2004; Alvarez et al., 2010); however, a detailed discussion on this absorption type is gathered to continuation.
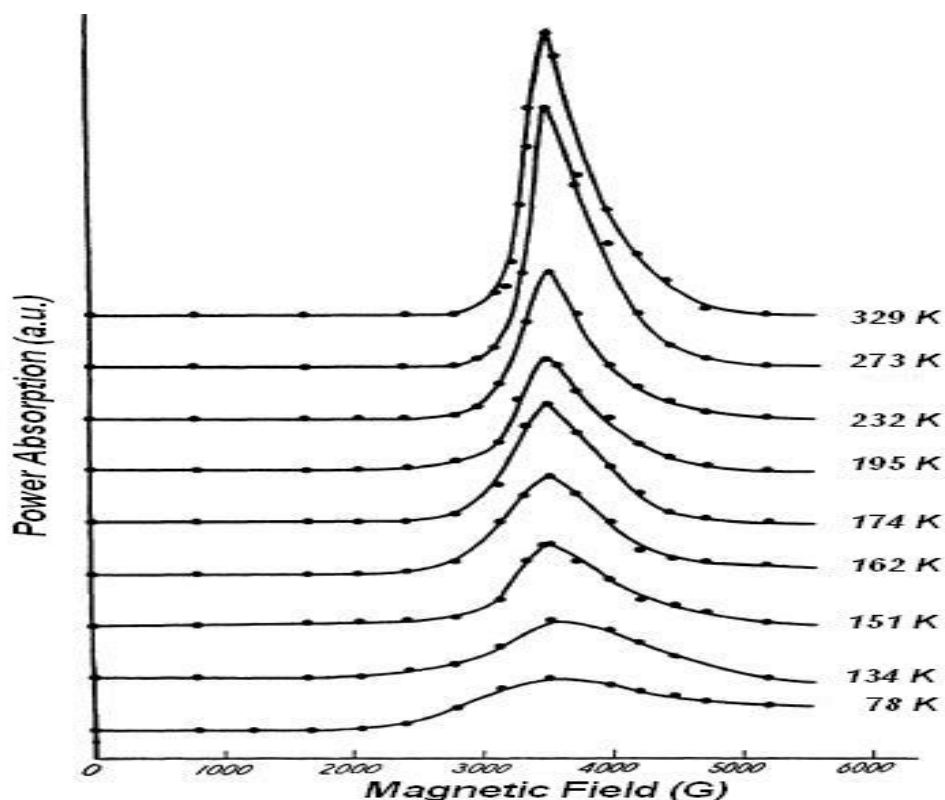

Figure 1. Direct resonance absorption versus dc magnetic field at 9.3 GHz for MnS around Néel transition (adapted from Okamura et al., 1951).
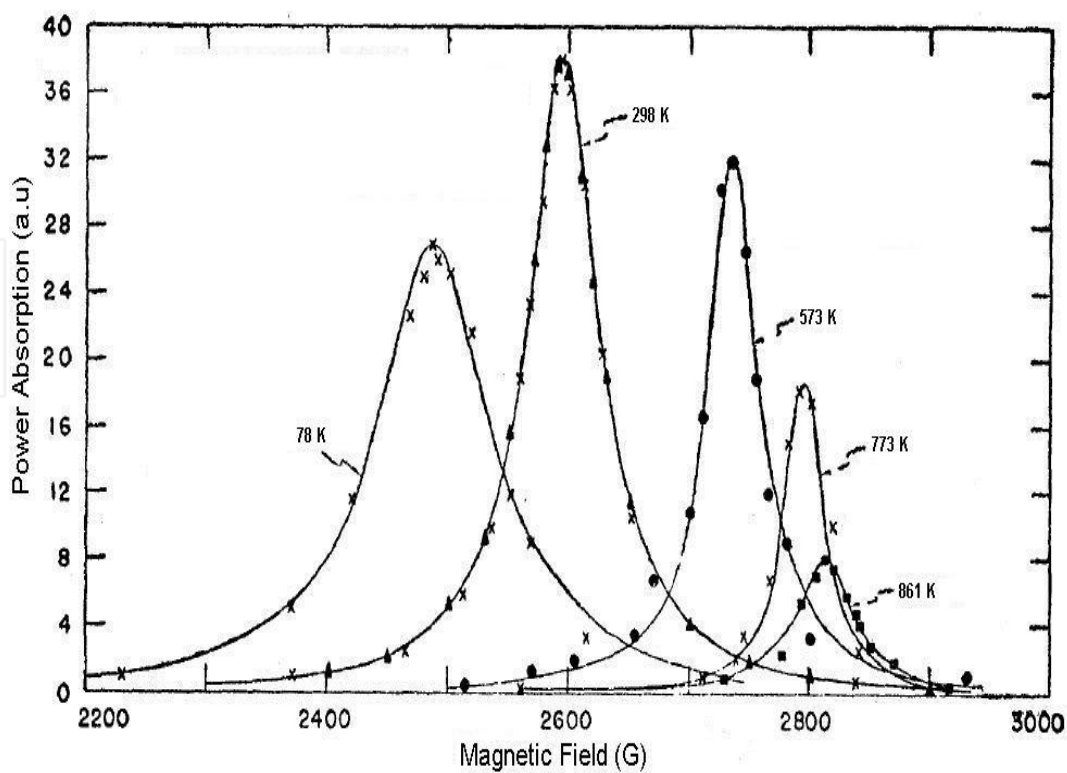
Figure 2. Direct resonance absorption versus dc magnetic field at 9 GHz in a sphere NiFe$_2$O$_4$ around Curie transition (adapted from Healy, 1952).
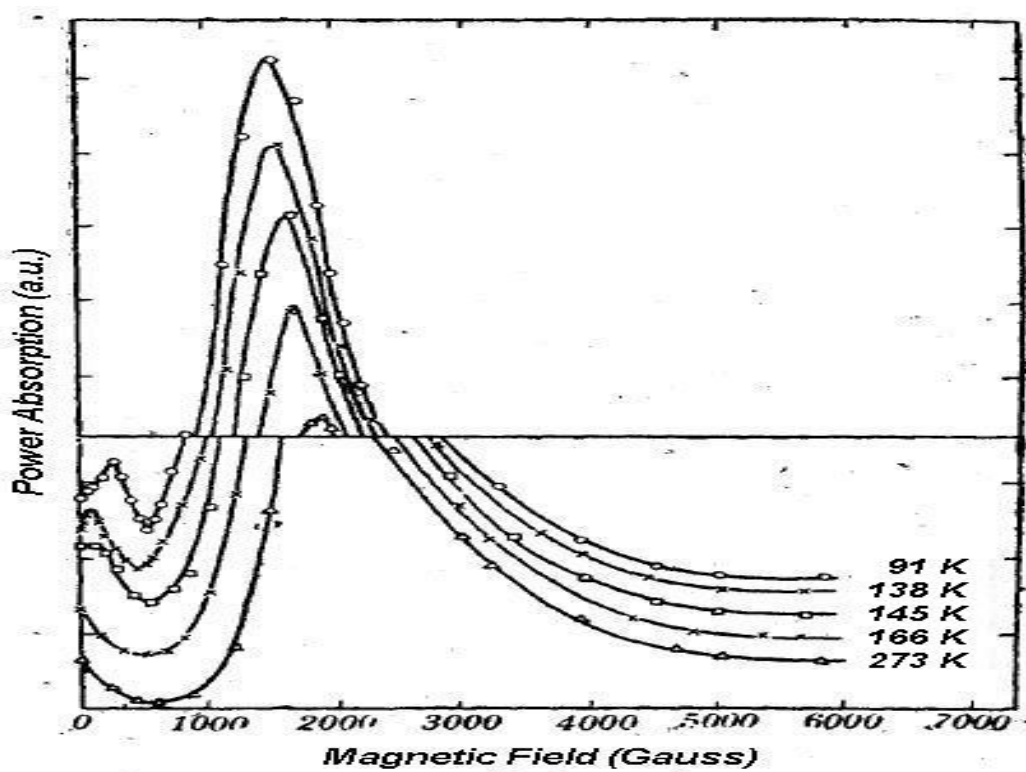

Figure 3. Direct resonance absorption versus dc magnetic field at 9.3 GHz for a disk NiFe$_2$O$_4$ at low temperature (adapted from Okamura, 1951).

The non-resonant microwave absorption (NRMA) was used in 1987 to detect the transition between the normal state and superconducting state in high-T_c superconductor ceramics (Bhat et al., 1987; Blazey et al., 1987; Bohandy et al., 1987; Khachaturyan et al., 1987; Moorjani et al., 1987). This was followed by a large number of reports on not only high-T_c superconductor ceramics (Kim et al., 1993; Topacli, 1996, 1998; Velter-Stefanescu et al., 1998, 2005; Padam et al., 1999, 2010; Shaltiel et al., 2001; Alvarez & Zamorano, 2004), but also including organic superconductors (Zakhidov et al. 1991; Bele et al., 1994; Hirotake et al., 1997; Niebling et al., 1998; Stankowski et al., 2004), the conventional superconductors of type-I and type-II (Kheifets et al., 1990; Bhide et al., 2001; Owens et al., 2001; Andrzejewski et al., 2004) and the newly discovered iron pniticide (Panarina et al., 2010; Pascher et al., 2010). Researches on NRMA have shown that this phenomenon is highly sensitive to detection of a superconducting phase in a material under study. The NRMA is usually detected as a function of a dc applied magnetic field or temperature, where these two variants are historically known as the magnetically-modulated microwave absorption spectroscopy (MAMMAS) and the low-field microwave absorption (LFMA), respectively.

In Fig. 4(a) is shown the MAMMAS response for bulk sample of the ceramic superconductor Bi-Sr-Ca-Cu-O around the superconducting transition. This response shows a level of absorption constant from 300 K to T_{on}= 81.5 K, and suddenly this signal rises sharply until T_{max}=63.6 K; at that temperature the superconducting transition has been completed. As temperature goes down from T_{max}, the superconductor sample enters more and more into the mixed state with a rigid fluxon lattice, and a decrease in the microwave absorption is observed. Fig. 4(b) shows LFMA spectra for selected temperatures, in a bulk sample of the ceramic superconductor Bi-Sr-Ca-Cu-O, where a hysteresis loop is observed in the superconductive state; since the microwave induced dynamics of the fluxon is dissipative, the field sweep cycle in LFMA measurement shows a hysteresis. The physical meaning of this hysteresis has been amply discussed by Topacli (1998) and Padam et al. (1999). For T$\geq$ 63 K, a non-hysteretic LFMA signal is observed and which goes disappearing when increasing the temperature, i.e. when the sample enters to normal state. The above-mentioned is a striking example of that the transition to the superconductive state in superconductor ceramics leads to NRMA. Additionally, it is recognized that NRMA is due mainly to the dissipative dynamics within Josephson junctions and/or to induced currents through weak links in superconductor materials.

Today, it is safe to assume that all superconductor materials exhibit a NRMA, and which has been experimentally confirmed; but the reverse statement, that any material that exhibits a NRMA is a superconductor, in general is not true. The NRMA may be caused not only by superconductivity, but also by any phenomena associated with magnetic-field-dependent microwave losses in the materials, and it can be employed to detect the magnetic transitions (Nabereznykh & Tsindlekht, 1982; Owens, 1997; Alvarez & Zamorano, 2004; Montiel et al., 2004; Alvarez et al., 2007, 2009, 2010). Some antecedent studies are given in the following. Nabereznykh & Tsindlekht (1982) have reported a study of NRMA in nickel near the Curie transition (Fig. 5), and in particular, they have employed LFMA measurements for detecting
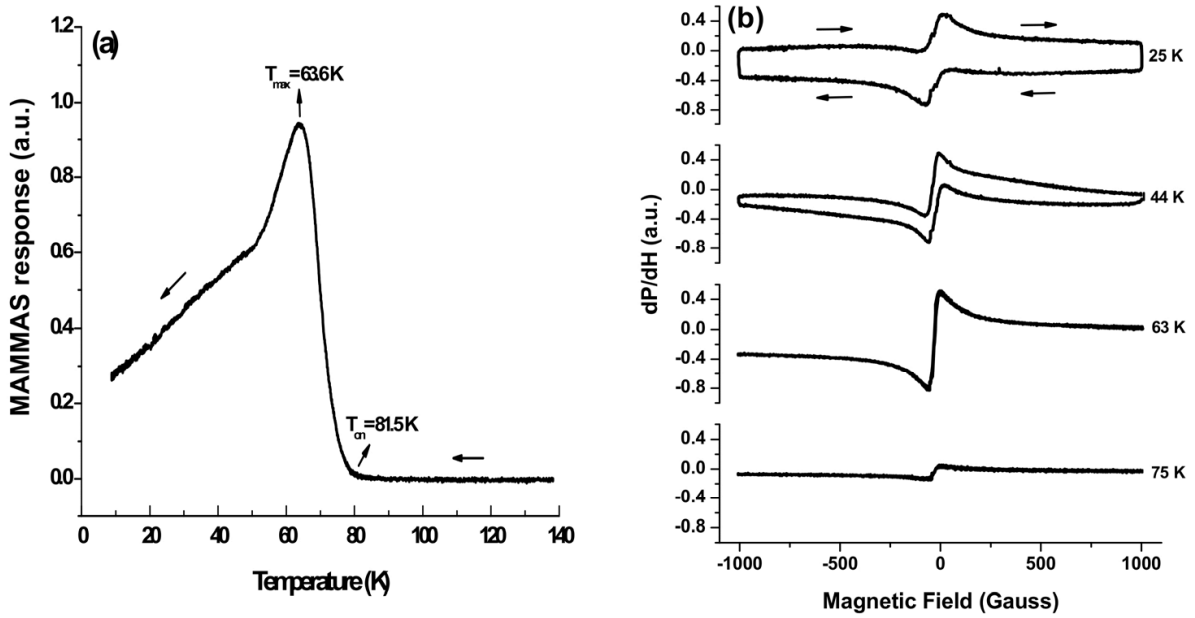
Figure 4. (a) MAMMAS response and (b) the LFMA spectra of a bulk sample of the ceramic superconductor Bi-Sr-Ca-Cu-O in the region of the superconducting transition.

the magnetic transition from a ferromagnetic order to paramagnetic phase. They suggest that the LFMA signal is due to the presence of a domains structure in the magnetic material. LFMA signal is highly distorted at T=571 K and at T=587 K it is completely inverted. At T= 601 K, the line intensity reaches its maximum, see Fig. 5; and when increases the temperature their intensity and width (ΔH_{LFMA}) diminishes. For T$\geq$ 630.9 K, a LFMA line is observed and it agrees with the value of the Curie temperature given in the literature for nickel, $\cong$ 630 K; suggesting that ΔH_{LFMA} is determined by the magnetic anisotropy field and the demagnetizing field.
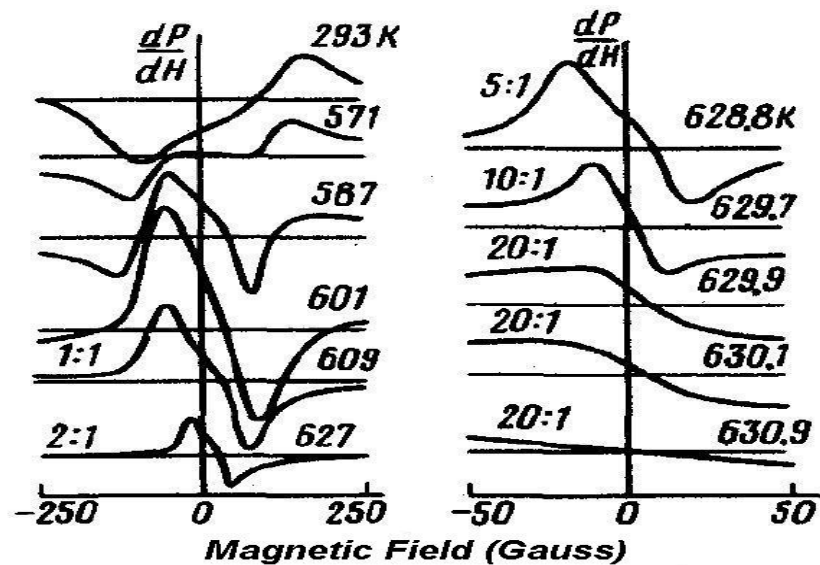
Figure 5. LFMA spectra in nickel for selected temperatures around Curie transition (adapted from Nabereznykh & Tsindlekht, 1982).

Other antecedent study is the detection of the Curie transition in a material with colossal magneto-resistance (CMR), as is La$_{0.7}$Sr$_{0.3}$MnO$_3$ manganite (Owens, 1997). The presence of the NRMA is evidence of the existence of a ferromagnetic order, i.e. this signal is not present in the paramagnetic phase and emerges as the temperature is decreased below Curie temperature, see Fig. 6; providing a sensitive detector of ferromagnetism. In Fig. 6(a), MAMMAS response shows the appearance and the rapid increase of the microwave absorption at ferromagnetic transition. Additionally, the half LFMA spectrum at 144 K in the ferromagnetic phase of La$_{0.7}$Sr$_{0.3}$MnO$_3$ is shown in Fig. 6(b). Owens (1997) suggests as a possible explanation of the origin of LFMA signal, the fact that the permeability in the ferromagnetic phase at constant temperature depends on the applied magnetic field, increasing at low fields to a maximum and then decreasing. Since the surface resistance of the material depends on the square root of the permeability, the microwave absorption depends non-linearly on the strength of the dc magnetic field, resulting in a NRMA centered at zero magnetic field.
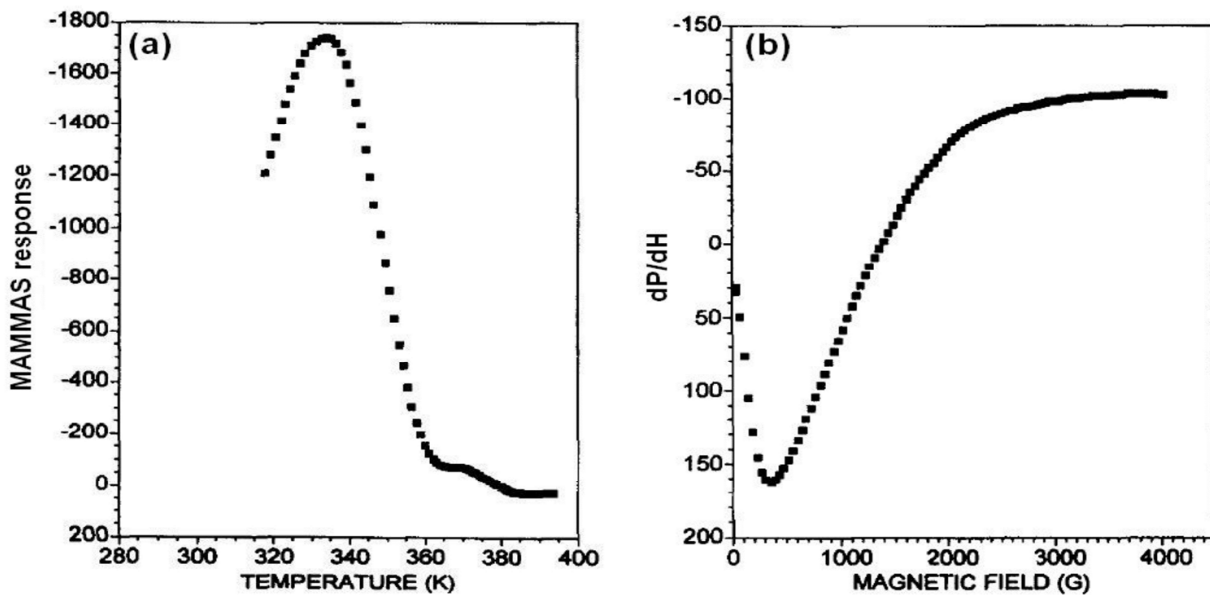

Figure 6. (a) MAMMAS response and (b) the half LFMA spectrum at 144 K in a bulk sample of La$_{0.7}$Sr$_{0.3}$MnO$_3$ manganite (adapted from Owens, 1997).

In this chapter, the changes in the EMR lineshape are studied for diverse magnetic materials in the 77-500 K temperature range; the different magnetic transitions are quantified by means of linewidth (ΔH_{PP}) and the resonant field (H_{res}) as a function of temperature. Through these studies we can distinguish the kind of present magnetic transition in the materials. Also, we employed the LFMA and MAMMAS techniques to give a further knowledge on magnetic materials, studying the different types of magnetic transitions and showing their main characteristics highlighted; we distinguish distinctive features associated with the microwave absorption by the magnetic moments and discuss on usefulness of these techniques as powerful characterization methodologies.

2. Experimental methods

In this work, the resonant and non-resonant microwave absorptions in several magnetic materials are studied around magnetic transitions. EMR technique measures the resonant microwave absorption as a function of dc magnetic field. Additionally, the NRMA measurements as a temperature function or an applied dc magnetic field are experimentally denominated as MAMMAS and LFMA, respectively.

2.1. Resonant microwave absorption measurement (EMR technique)

The basic components of a standard EMR spectrometer are shown in Fig. 7. In a sample placed at center of a microwave cavity (see Fig. 8), an applied dc magnetic field is increased until that the energy difference between the spin-up and spin-down orientations, match the microwave frequency of the power supply; where a strong absorption is clearly detected. For this type of spectrometer, the derivative of microwave absorption (dP/dH) as a magnetic field function is plotted.
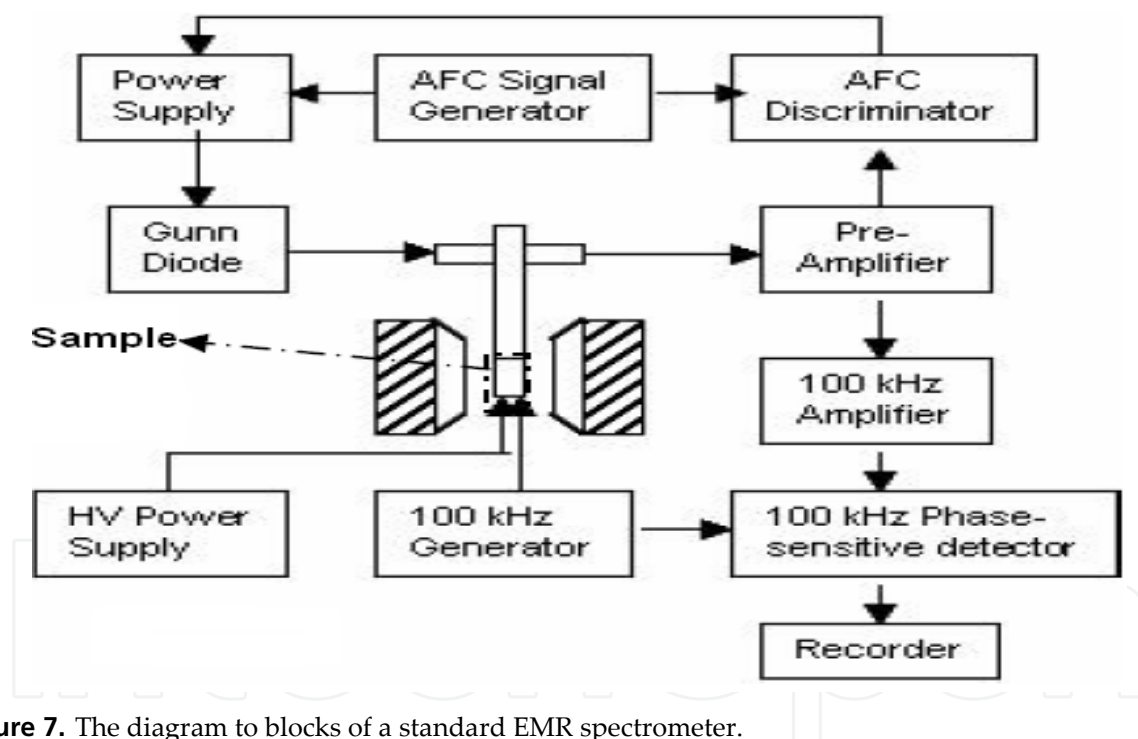

Figure 7. The diagram to blocks of a standard EMR spectrometer.

We give a description detailed of the EMR spectrometer (Jeol JES-RES3X). In a T-magic bridge, the microwaves (H_{mw}), with power P_0 and frequency ν_{mw}= 8.8-9.8 GHz (X-band), are generated by a JEOL/ES-HX3 microwave unit and are fed to the cylindrical cavity (see Fig. 8) through a rectangular wave-guide; coupling adjuster of the cavity must be adjusted so that no wave is reflected from the cavity. The absorption of the microwave energy by a sample generates a change in the quality factor (Q) of the cavity; due to this change, the microwave bridge becomes non-balanced, causing that a wave is reflected from the cavity. The change in cavity Q-factor is due to changes in the energy absorption resonant by spins.

The reflected waves from the cavity (P_{ref}) with the information of the microwave absorption by the sample are directed towards a detector crystal, which was previously biased to a 10% of the incident power in order to work in the linear regime; with this method of detection-homodyne and lock-in amplification, a very high sensitivity in the measurements is guaranteed.
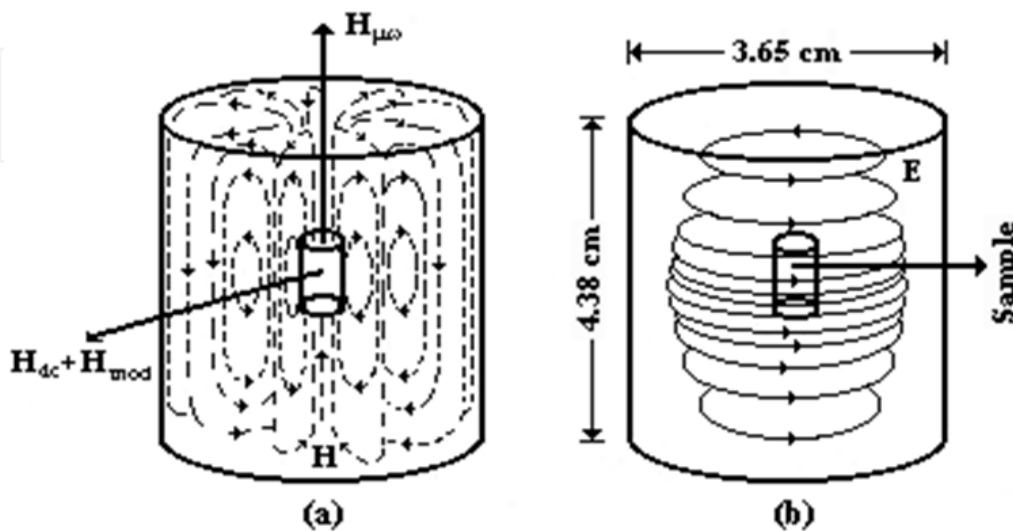

Figure 8. Distribution of (a) magnetic and (b) electric fields, and the sample location inside the TE_{011} cylindrical cavity in the JEOL JES-RES 3X spectrometer.

The sample is subjected to a dc magnetic field (H_{dc}), that it is produced by an electromagnet with truncated pole pieces, and a weak ac magnetic field (H_{mod}) is superimposed to H_{dc}. The H_{mod} is achieved by placing small Helmholtz-coils on each side of the cavity along the axis of the static field, which are fed and controlled by a sign generator. The amplitude of this field goes from 0.002 G to 20 G with a modulation frequency of 100 kHz, thus allowing, the microwave absorption registration at the modulation frequency. In EMR measurements, H_{dc} could be varied from 0 to 8000 G.

2.2. NRMA measurements (LFMA and MAMMAS techniques)

The Jeol JES-RES3X spectrometer was modified (see Fig. 9), connecting the output of a digital voltmeter (signal Y) to a PC enabling digital data acquisition (Alvarez & Zamorano, 2004); where this electrical signal is proportional to NRMA from sample. The signal Y is fed to a 7½ digits - Keithley DMM-196 voltmeter. Hence, the reading of this voltmeter (V_y) carries the information of the microwaves absorption by sample.

LFMA technique measures the NRMA as a function of H_{dc}, this uniform field is produced by the same electromagnet, but which receives current regulated from two power supplies (JEOL JES-RE3X and ES-ZCS2); and they are synchronized to obtain a true zero-value of the magnetic field between the pole caps. The Jeol ESZCS2 zero-cross sweep unit compensates digitally for any remanence in the electromagnet, with a standard deviation of the measured field of less than 0.2 G, allowing measurements to be carried out by cycling the H_{dc} about its

zero-value continuously from -1000 G to +8000 G. Hence, symmetric field-sweeps from ±0.1 G to ±1000 G are available and asymmetric field-sweeps up to $-1000\ G \leq H_{dc} \leq 8000\ G$ are also available in order to detect possible hysteresis for NRMA signal, and which would point out to irreversible processes of microwave energy absorption. In this technique, the sample is zero field cooled or heated to the fixed temperature. For our studies, the temperature is maintained fixed with a maximum deviation of 1 K during the whole LFMA measurement (<8 min of sweeping). The magnetic field is swept following a cycle; the field sweep schemes have their analog in the magnetic hysteresis measurements. GPIB port of a PC receives the magnetic field coming from the Group3 DTM-141 teslameter, and it is displayed as the X-axis on the plot of the data being acquired; meanwhile, the voltmeter V_y receives the NRMA signal. Then, what is measured is not the microwave power absorption itself, but rather its derivative with respect to magnetic field (dP/dH). This allows us to distinguish the field-sensitive part of the microwave absorption from the part that does not depend on magnetic field, and record only the first; and also, to use narrow-band amplifier to enhance the signal, which greatly increases the signal-to-noise ratio.
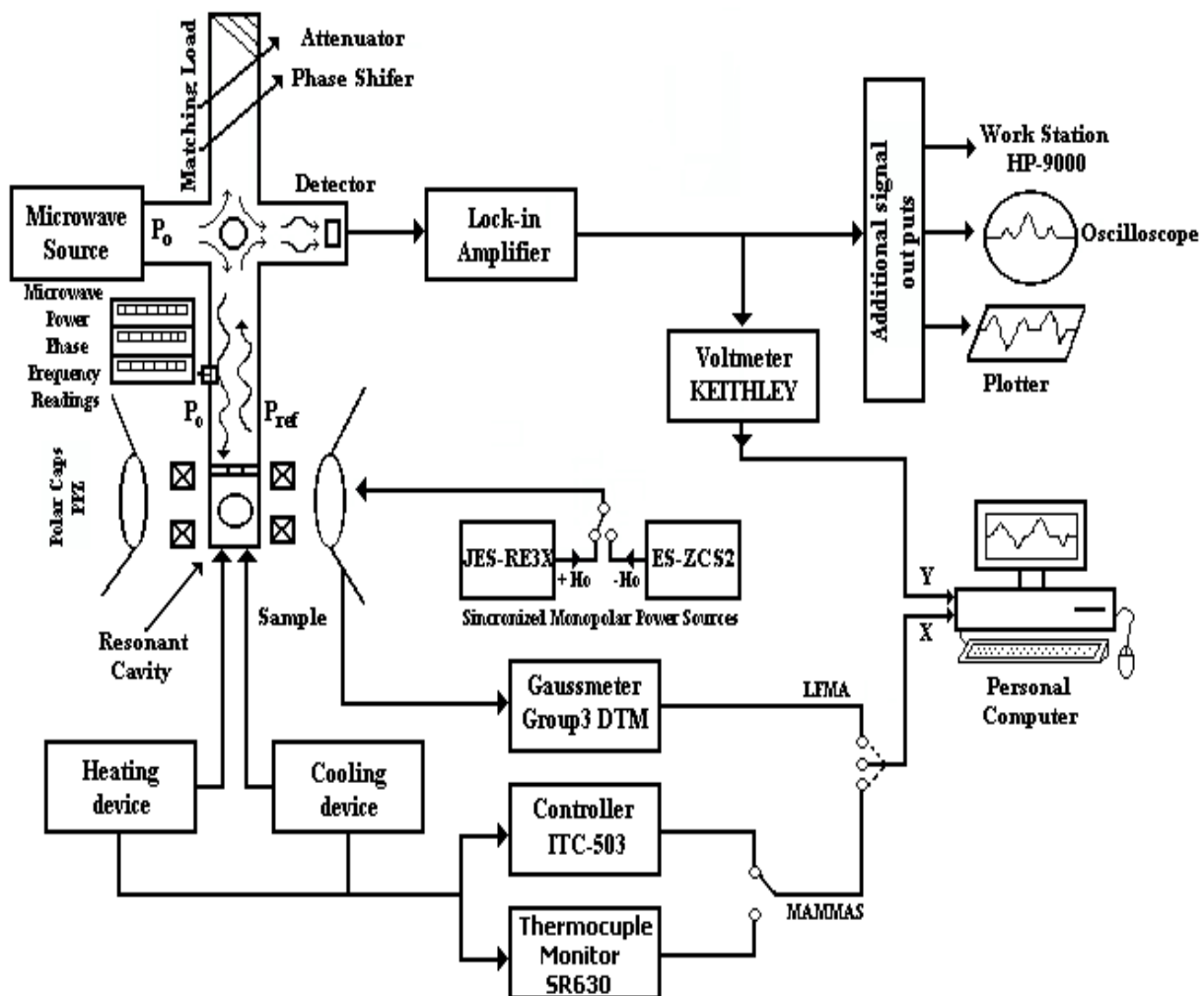

Figure 9. Block diagram of LFMA and MAMMAS techniques (adapted from Alvarez & Zamorano, 2004).

MAMMAS technique allows measurement as a temperature function, giving information on the temperature profile of NRMA response of each material and can also provide valuable information about the nature of magnetic ordering in the materials. The temperature of the sample is slowly varied (~1 K/min) and controlled by flowing N_2 gas through a double walled quartz tube, which is inserted through the center of the microwaves cavity, in the 77-500 K temperature range. The temperature is measured by a copper constantan thermocouple placed inside the sample tube just outside the cavity. Its output signal is further digitized by means of the Stanford SR630 thermocouple monitor. In this technique, the temperature is plotted along the X-axis, and the microwaves absorbed by the sample are collected as V_y and are plotted along Y-axis.

3. EMR and NRMA studies in magnetic transitions

In this section, we show several EMR and NRMA studies in diverse magnetic materials through magnetic transitions. These examples include: the amorphous ribbon $Co_{66}Fe_4B_{12}Si_{13}Nb_4Cu$, the ferrite $Ni_{0.35}Zn_{0.65}Fe_2O_4$ and the magnetoelectric $Pb(Fe_{2/3}W_{1/3})O_3$; highlighting their main characteristics and illustrating how magnetic transitions are manifested in this kind of measurements.

3.1. Curie transition (from a ferromagnetic order to paramagnetic phase)

We show several studies in amorphous ribbons of nominal composition $Co_{66}Fe_4B_{12}Si_{13}Nb_4Cu$ and dimensions of 2 mm wide and 22 μm thick, which were prepared by the melt-spinning method; where their initial amorphous state was checked by X-ray diffraction (XRD). All the measurements were performed in the 300-500 K temperature range.

3.1.1. EMR technique

These measurements were carried out from -1000 G to 8000 G, with forward and backward H_{dc} sweeps in order to detect reversible and/or irreversible microwave absorption processes. At 300 K, two microwave absorptions were observed: the first absorption to high magnetic field (~1469 G) corresponding to an EMR spectrum, and other absorption at low magnetic fields around zero (LFMA signal). Fig. 10 shows the derivative of microwave absorption, and which consists of an EMR spectrum and a LFMA signal; additionally a DDPH pattern of paramagnetic nature is also included.

We will only center ourselves in EMR absorption, associated with the ferromagnetic resonance (FMR). This absorption satisfies the Larmor condition; when is applied to the case of a thin sheet with both negligible anisotropy field and the demagnetizing fields (Yildiz et al., 2002),

$$w = \gamma[(4\pi M + H_{efec}) \cdot H_{efec}]^{1/2} \tag{1}$$

where ω is the microwave angular frequency (with ω = 2πf and f = 9.4 GHz), γ is the gyromagnetic ratio, H_{efec} is the effective magnetic field and M is the magnetization. The
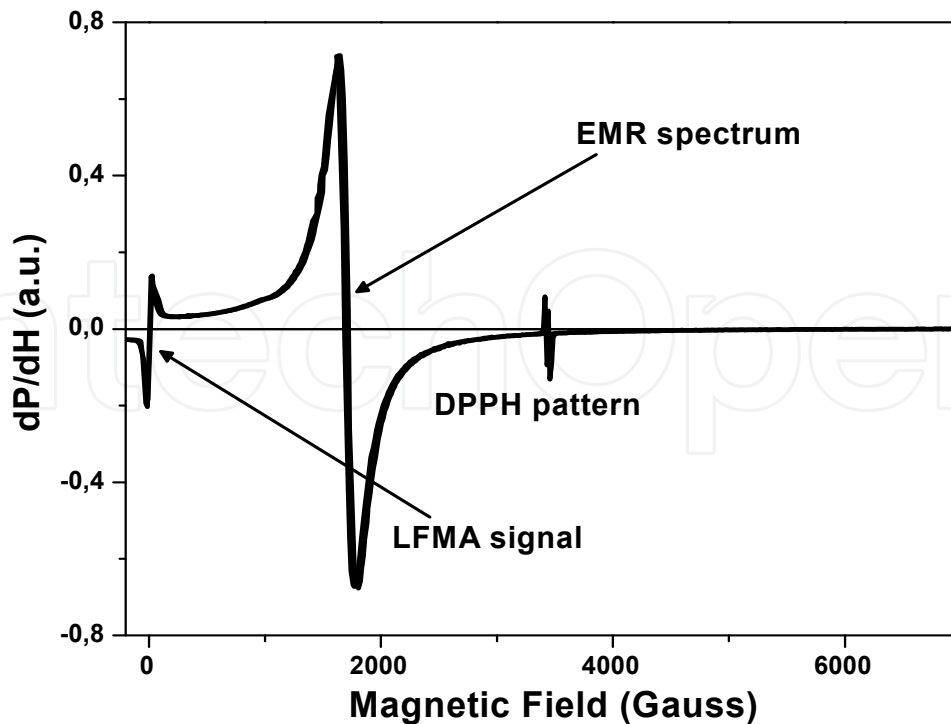
Figure 10. The derivative of microwave absorption from -1000 G to 8000 G, and which consists of an EMR spectrum and a LFMA signal (adapted from Montiel et al., 2005).

resonant condition implies that $M=M_s$ with $H_{efec}= H_{dc}+H_{int}$, where H_{int} is the internal field. The saturation magnetization of the surface of the sample can be calculated from the resonance conditions as $4\pi M_s = 4741$ G; which is close to the bulk saturation magnetization $4\pi M_s=5250$ G, the difference can be attributed to the fact that FMR is probing only the surface of the sample. Additionally, this absorption shows no hysteresis between the forward and backward field sweeps.

In Fig. 11, the temperature dependence of the EMR spectra can be observed. As temperature increases ΔH_{pp} becomes wider, due to new magnetic processes; where the dominant process is the dipole-dipole interaction associated with the paramagnetic phase, while the exchange interaction of the ferromagnetic order disappears when increasing the temperature. The dipole-dipole interaction has the effect of increasing the linewidth, while exchange interaction tends to narrow the absorption line. ΔH_{pp} as temperature function is shown in Fig. 12(a), the Curie temperature ($T_c=482$ K) is associated with the inflection point; where the derivative of the linewidth exhibited a maximum at T_c. A second EMR spectrum (SES) is detected after the magnetic transition, and it is associated with a second magnetic phase with a different Curie temperature; where this absorption mode is due to a nanocrystalline phase. The conductive behavior decreases due to the temperature increase, consequently, the absorption centers diminish and the EMR lineshape starts to become symmetrical. Also, the gain is one order of magnitude greater than at room temperature, and it is indicative of a reduced number of absorbing centers in the paramagnetic phase due to the high entropy of the system. Additionally, the temperature dependence of the resonant field is plotted in Fig. 12(b), where a shift in the resonant field is clearly observed. At 300 K, in ferromagnetic

order, H_{res} corresponds to $H_{efec}= H_{dc}+H_{int}$, and as temperature increase H_{int} diminishes until $H_{int}=0$ at $T_c=482$ K in paramagnetic regime, with $H_{efec}= H_{dc}$.
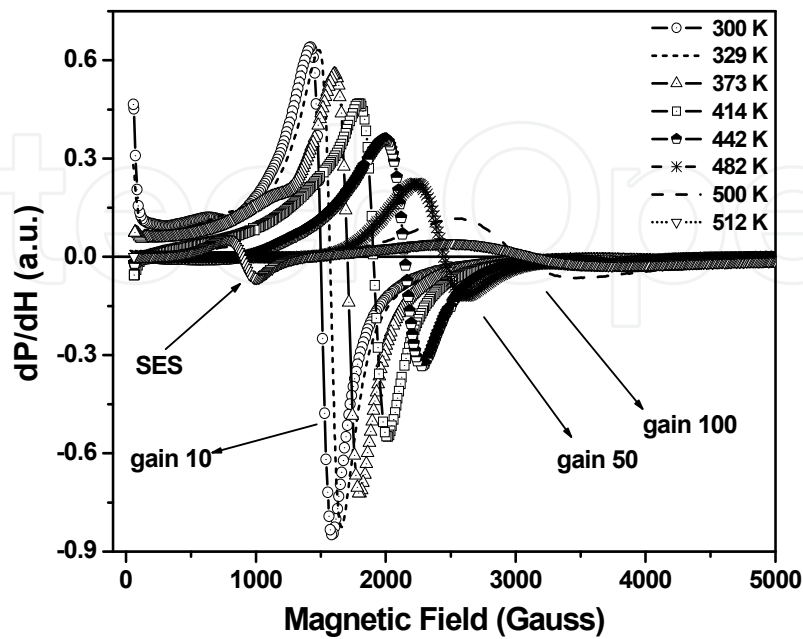

Figure 11. EMR spectra at different temperatures in amorphous ribbon $Co_{66}Fe_4B_{12}Si_{13}Nb_4Cu$; where the Curie temperature is detected at 482 K, and a decrease in microwave absorption is observed after magnetic transition.
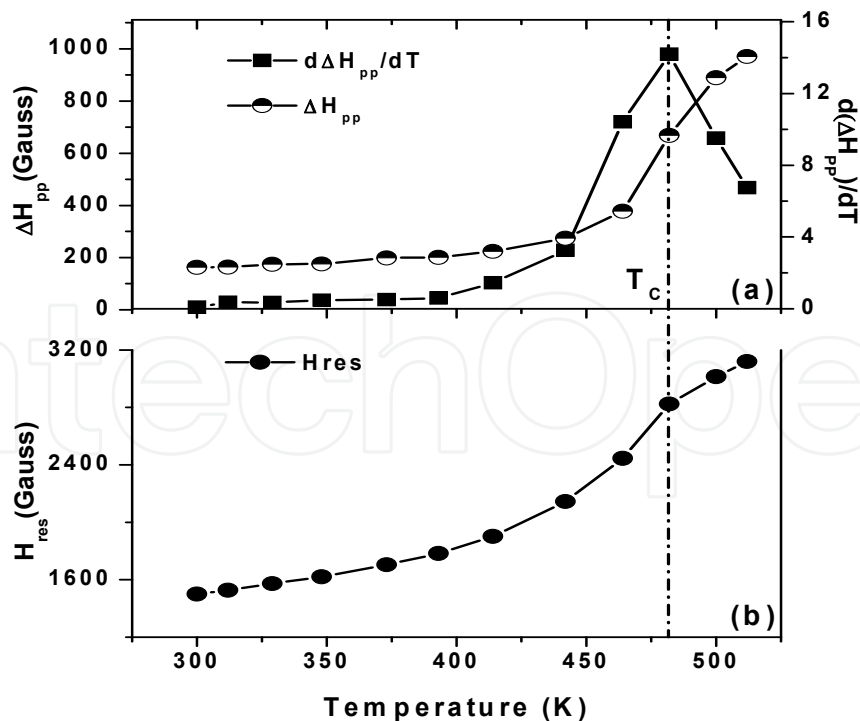

Figure 12. Temperature dependence of (a) ΔH_{pp} and (b) H_{res} in the amorphous ribbon $Co_{66}Fe_4B_{12}Si_{13}Nb_4Cu$ for EMR spectrum; solid lines are guides for the eye only. Also, Fig. 12(a) shows the derivative of ΔH_{pp} with the temperature, showing a maximum to Curie temperature.

3.1.2. LFMA technique

LFMA signal in amorphous ribbon is shown with more detail in Fig. 13(a). This signal is centered at zero magnetic field and shows an opposite phase to the EMR spectrum. The opposite phase is undoubtedly indicating that the microwave absorption has a minimum value at zero magnetic field, in contrast to the maximum value for EMR spectrum. LFMA signal has been interpreted as due to low-field spin magnetization processes (Beach & Berkowitz, 1994; Domínguez et al., 2002). We have correlated the LFMA signal with magnetoimpedance (MI) phenomena (Montiel et al., 2005), where Fig. 13(b) shows the MI response at 50 MHz for amorphous ribbon. The double peak clearly indicates low-field surface magnetization processes (Beach & Berkowitz, 1994) originated by the change in transversal permeability. The peak-to-peak width in MI is associated with the anisotropy field (H_K). In addition, Fig. 13(c) shows magnetometry measurements. The hysteresis loop is characterized by axial anisotropy, and a correlation between both experiments is observed on the basis of H_K. We compare measurements of LFMA, MI and magnetometry, in Fig. 13. A significant decrease of the microwave absorption (from H=16 G down to zero) is observed in LFMA measurements, whereas at the same fields, the magnetoimpedance measurement show that MI response is approaching saturation at field lower than 20 G. As the field decreases, a maximum is reached by MI, which corresponds to the anisotropy field (H=15.6 G). A further decrease of impedance is observed at zero field. As it is well known, MI is due to changes in the skin depth as a consequence of changes in the transversal permeability under the influence of the external H_{dc}. The change in domain structure, and therefore in spin dynamics, is also produced by H_{dc}, in a direct interaction with the axial anisotropy of the material. Experimentally, the maxima in MI signal coincide with the minimum and maximum of the LFMA signal and it can be associated with a common origin for both phenomena, where the magnetic processes in both phenomena are dependent of H_K.

The hysteresis effect of the LFMA signal appears to be due to a non-uniform surface magnetization processes. A ferromagnetic conducting system can absorb electromagnetic radiation energy and the efficiency of this absorption depends on the particular conditions such as: the magnetic domain structure, magnetic anisotropy, the orientation of the incident propagation vector radiation, its conductivity, its frequency and amplitude. This absorption can easily be modified by H_{dc}, which changes the magnetic susceptibility, the penetration depth, the magnetization vector, the domain structure and spin dynamics. Such changes can show hysteresis, as normally occurs in a domain structure subjected to dc fields lower than the saturating field. By cycling the H_{dc}, different irreversible domain configurations occur, and therefore a hysteresis effect can be obtained. These results clearly suggest that MI effect and LFMA signal represent the same responses to an external H_{dc}. MI and LFMA are due to domain structure and spin dynamics, and they can be understood as the absorption of electromagnetic energy by spin systems that are modified by domain configuration and strongly depends on H_K.

Let us consider an electromagnetic wave with both electric (**E**) and magnetic (**H**) fields. The time-average density of the power absorption (P), for a ferromagnetic conductor at high frequencies, can be expressed by the complex Poynting vector as: P=½Re[**E**×**H***] or
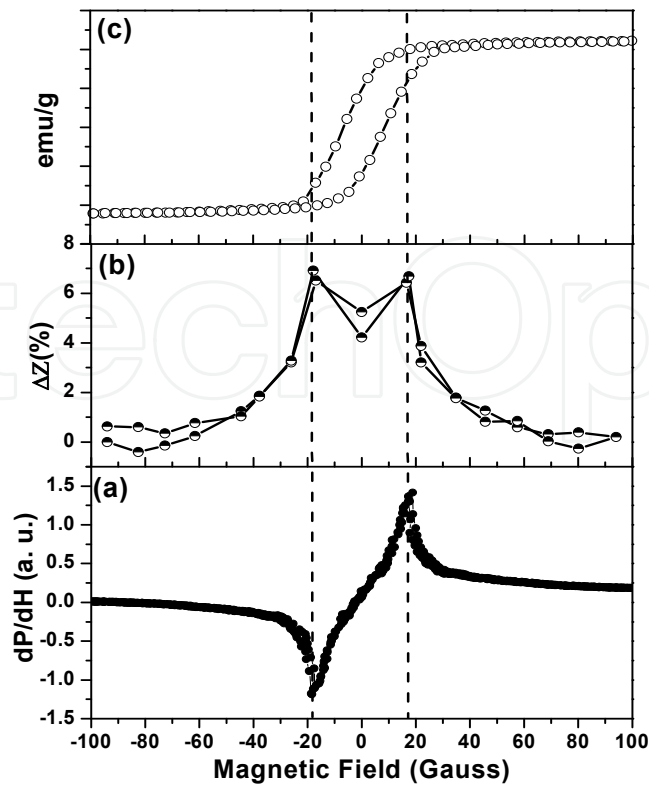
Figure 13. (a) LFMA signal, (b) MI signal at frequency of 50 MHz, and (c) VSM hysteresis loop for the amorphous ribbon $Co_{66}Fe_4B_{12}Si_{13}Nb_4Cu$ (adapted from Montiel et al., 2005).

P=½Re[E·H*], where **H*** is the complex conjugate of **H**, and Re[x] the real part of the operator. Additionally, the ac surface impedance for a ferromagnetic conductor material is defined as the ratio of the fields at the surface: Z=E_s/H_s. Then the time-average density of the microwave power absorption can be written as P=½H_s^2Re(Z). The ac magnetic field H_s, in a ferromagnetic conductor at high frequency, is generated by a uniform current j=σE_s (with σ the electrical conductivity) induced by the ac electric field E_s; and therefore H_s is constant to changes of an applied static magnetic field.

Therefore, we can establish a relation between the field derivative (dP/dH) of the microwave power absorption and the rate of change of Re (Z) with an applied static magnetic field, H:

$$dP / dH = \left(H_s^2 / 2\right)\left[dRe(Z) / dH\right]$$ (2)

For a good magnetic conductor Z= (1+j)/$\sigma\delta$, with the classical skin depth 1/δ= ($\omega_0\mu\sigma$/2)$^{1/2}$ and μ the permeability. The magnetoimpedance is defined as the change of the impedance of a magnetic conductor subjected to an ac excitation current, under the application of a static magnetic field H_{dc}; it is a very similar phenomenon to the one involved in the microwave power absorption. At high-frequencies (microwaves) and due to the skin depth effect, only the surface impedance is involved.

LFMA signal can be used to detect magnetic order and to determine Curie temperature, because the appearance of LFMA signal has been widely accepted as a signature of the onset

of the ferromagnetic transition (Montiel et al., 2004; Alvarez et al., 2010; Gavi et al., 2012). Therefore, it is possible to establish that for temperatures above the Curie temperature, the long-range magnetic order is completely lost and LFMA signal disappears. LFMA signal shows a decrease in the intensity as temperature is approached to T_c, and finally disappeared at $T \geq T_c$. Fig. 14 shows the temperature dependence of the LFMA signal, it is necessary to mention that LFMA signal is located around zero field for all temperatures. At room temperature, the LFMA signal has a phase opposite to EMR spectrum. As temperature increases, for $T \geq 373$ K, LFMA signal invests its phase until disappearing. This behavior is correlated with the long-range order in the ferromagnetic state and with the temperature dependence of the anisotropy field. The phase change has been observed previously in nickel around Curie transition, Nabereznykh & Tsindlekht (1982), and it can be explained by means of magnetic fluctuations; and they are associated with the electric properties of the material. LFMA signal showed a decrease in ΔH_{LFMA} and hysteresis remains until T_c is reached.
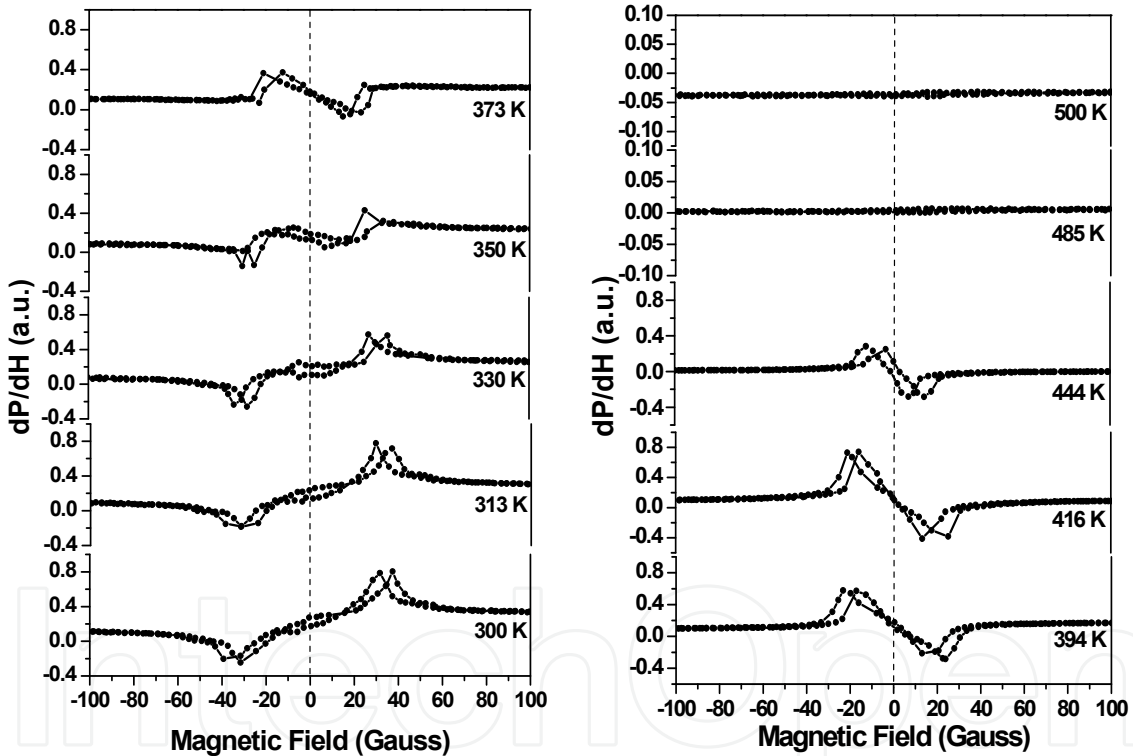

Figure 14. LFMA signals at different temperatures in the amorphous ribbon $Co_{66}Fe_4B_{12}Si_{13}Nb_4Cu$. At 485 K the LFMA signal disappears, indicating the transition from the ferromagnetic order to paramagnetic phase.

3.2. Curie and Yafet-Kittel transitions (from ferrimagnetic order to a Yafet-Kittel-type ordering)

The polycrystalline Ni-Zn ferrites ($Ni_{1-x}Zn_xFe_2O_4$, $0 \leq x \leq 1$) are an important family of solid solutions with a remarkable variety of magnetic properties and applications

(Ravindaranathan et al., 1987). This solid solution crystallizes in a cubic spinel-type structure, see Fig. 15(a), where Zn ions normally are located in tetrahedral sites (A-sites) and Ni ions have a marked preference to occupy the octahedral sites (B-sites), while Fe ions are distributed among both sites types. The antiferromagnetic superexchange interaction (A-O-B) is the main cause of the cooperative behavior of the magnetic moments in Ni-Zn ferrites below their Curie temperature. In a great variety of experimental observations (Satya Murthy et al., 1969; Pong et al., 1997; Akther Hossain et al., 2004) have found that for x≤0.5 the resultant of the magnetic moments in the A and B sites has a classic collinear arrangement, see Fig. 15(b); while that for x>0.5 a non-collinear arrangement of the magnetic moments is employed to explain these behaviors. The previous behaviors are because the superexchange interaction B-O-B begins to be comparable with A-O-B interaction, and the arrangement of the magnetic moments shows a Yafet-Kittel-type canting (Yafet & Kittel et al., 1952). Also, the transition temperature from a ferrimagnetic ordering (collinear arrangement) to a Yafet-Kittel-type magnetic ordering (non-collinear arrangement) is called Yafet-Kittel temperature (T_{YK}); in particular, $Ni_{0.35}Zn_{0.65}Fe_2O_4$ ferrite has a T_{YK} smaller than the Curie temperature (Satya Murthy et al., 1969; Akther Hossain et al., 2004). The polycrystalline $Ni_{0.35}Zn_{0.65}Fe_2O_4$ ferrite was prepared by two different methods: the conventional classical ceramic method known as the solid-state reaction, and the co-precipitation method.
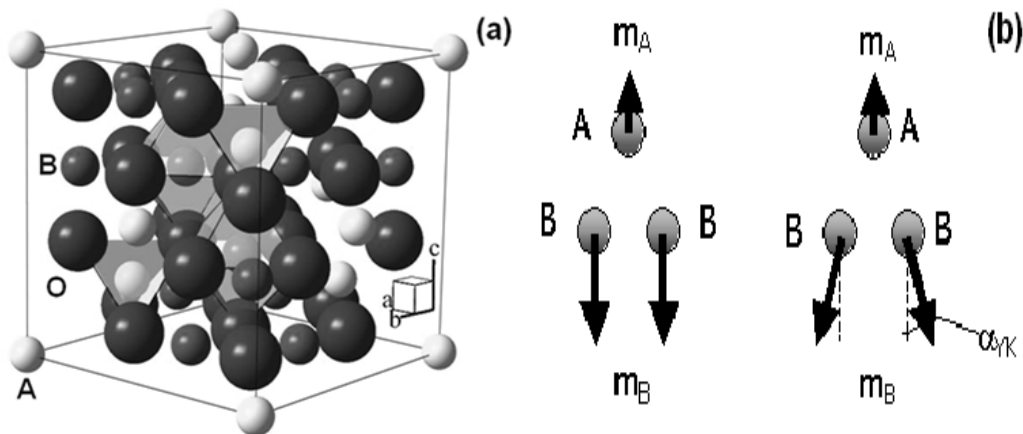

Figure 15. (a) Schematic representation of unit cell structure for Ni-Zn ferrites; where A and B are tetrahedral and octahedral sites, respectively. (b) Spin orientation on the A and B sites, for the collinear (to left) and the non-collinear (to right) model, in Ni-Zn ferrites; where α_{YK} is the Yafet-Kittel angle (adapted from Alvarez et al., 2010).

3.2.1. EMR technique

Fig. 16 shows the EMR spectra of the Ni-Zn ferrite prepared by solid-state reaction at different temperatures. For all temperature range, EMR spectra exhibit a broad signal, but their lineshape change with a shift in H_{res} when varying the temperature. Beginning to low temperature, an asymmetric mode (FMR signal) is observed and it gradually changes to a symmetric mode (EPR signal) when increasing the temperature. This change is associated

with the transition from a ferrimagnetic order to a paramagnetic phase; i.e. the evolution from a FMR spectrum to an EPR spectrum is used to determine the Curie temperature (T_c) in Ni-Zn ferrites (Montiel et al., 2004; Wu et al., 2006; Priyadharsini et al., 2009; Alvarez et al., 2010). Additionally, EMR spectra exhibit an additional absorption at low magnetic field, this new absorption mode is a LFMA signal which will be discussed with more detail in the following section.
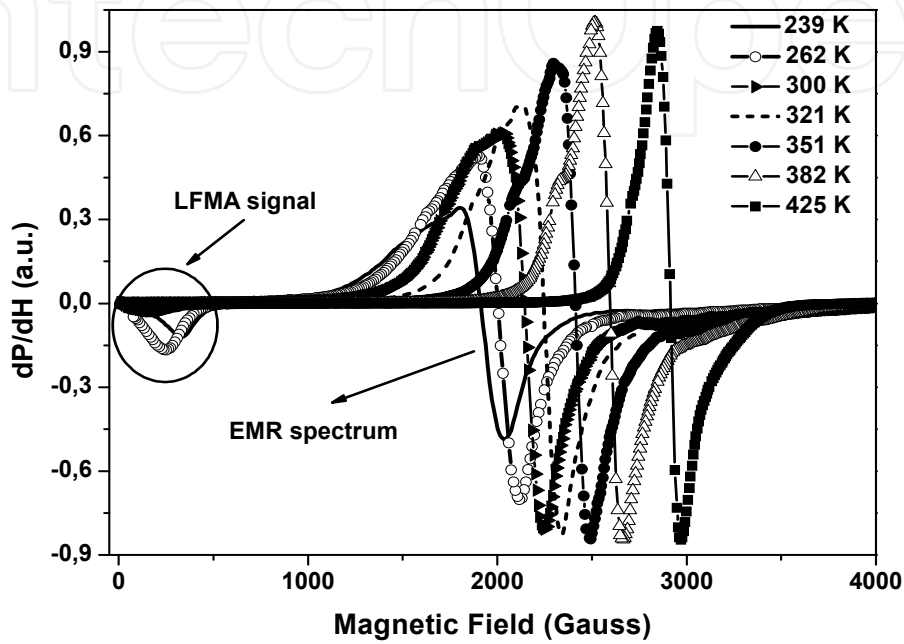

Figure 16. EMR spectra of the Ni-Zn ferrite prepared by solid-state reaction, for selected temperatures in the 239-425 K temperature range; circle shows LFMA signal.

In a polycrystalline magnetic material, the resonance condition for FMR signal is expressed as:

$$w = \gamma H_{res} \tag{3}$$

with $H_{res}=H_{dc}+H_{int}$, and H_{int} is the internal field which is the combination of several factors associated with the long-range order in the ferrite (Schlomann, 1958): the anisotropy field (H_K), the porosity field (H_P), the field due to eddy currents (H_e) and the demagnetization field (H_d). Additionally, the inhomogeneities in Ni-Zn ferrites also can contribute to internal field, and they are associated with differences in sites occupancy by cations. Other source of inhomogeneity in the internal field is the disorder in the site occupancy. Even if the occupancy of sites is well determined (i.e., in Ni-Zn ferrite, all Zn cations on A sites, all Ni cations on B sites), there can be an inhomogeneous distribution of each of them on the sites. EMR spectra can be slightly different when this occupancy of sites is not strictly homogeneous, since some terms of H_{int} are not exactly the same for all the absorbing centers. It is possible to change the cations distribution in the ferrites by means of thermal treatments or when preparing samples of the same composition but with different synthesis methods.

H_{res} as a function of temperature for the conventional and co-precipitate Ni-Zn ferrites are shown in Fig. 17(a). The values for conventional ferrite are lightly higher than those of the co-precipitate ferrite. This difference can be due to inhomogeneities associated with a different distribution of cations, and that it is originated by synthesis method. For both samples, the increment of H_{res} as temperature increases is due to decrement of the internal field, i.e. in the ferrimagnetic order H_{int} is added to the applied field and the resonance condition is reached at low values of H_{dc}. In contrast, in the paramagnetic phase, the necessary magnetic field to satisfy the resonance condition has to be supplied entirely by the applied field, $H_{int}= 0$ and $H_{res}= H_{dc}$; i.e. when increasing the temperature the progressive disappearance of H_{int} is associate with the lost long-range order.

ΔH_{pp} can be due to several factors (Srivastava & Patni, 1974), in particular for polycrystalline samples the linewidth is due to: the sample porosity (ΔH_{por}), the magnetic anisotropy (ΔH_K), the eddy currents (ΔH_{eddy}), and the magnetic demagnetization (ΔH_{des}). It is necessary to mention that there is a broadening due to variations in cations distribution on the A and B sites, and it is highly dependent of the preparation method. In Fig. 17(b), we show the behavior of ΔH_{pp} with temperature for the conventional and co-precipitate Ni-Zn ferrites. For all the temperatures, ΔH_{pp} in co-precipitate ferrite is higher than for the conventional ferrite. This behavior can be due to differences in the microscopic magnetic interactions inside the samples, mainly the interparticle magnetic dipole interaction and the superexchange interaction; and they are originated by different cations distributions in the samples, due to synthesis method. The magneto-crystalline anisotropy has a strong contribution to ΔH_{pp} and we can have the following approximation $\Delta H_{pp}=\Delta H_K=K_1/2M_s$, i.e. for a system of randomly oriented crystallites, the contribution of the anisotropy field is
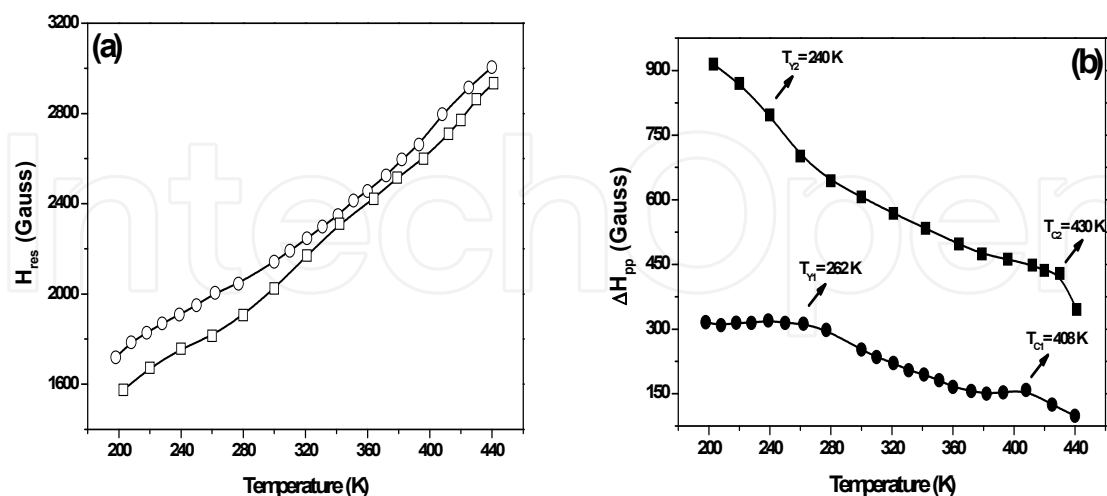

Figure 17. (a) Temperature dependence of H_{res} in the 200-440 K temperature range for the (○) conventional and (□) co-precipitate Ni-Zn ferrites. (b) Temperature dependence of ΔH_{pp} in the same temperature range for the (●) conventional and (■) co-precipitate Ni-Zn ferrites. The curves connecting points are only guides for the eye.

dominant. For both ferrites, the decrease in ΔH_{PP} as temperature increases is associated to a weakening of the magneto-crystalline anisotropy as T approaches T_c (Byun et al., 2000). The magnetic transition (ferri-paramagnetic) appears as an inflection point in plot ΔH_{PP} vs. temperature, as is shown in Fig. 17(b). The inflection points at $T_{c1} \sim 408$ K (conventional) and $T_{c2} \sim 430$ K (co-precipitate) are associated with Curie temperature of each sample. We observed that the Curie transition is higher in the co-precipitate Ni-Zn ferrite. As T_c is an intrinsic property, that it depends entirely on the ferrite composition, the difference in Curie temperature between both ferrites also suggests a different occupancy between the A and B sites. To high temperature, the long-range magnetic order is completely lost except for some short range order islands in the material that contribute strongly in the broadening of the EMR spectrum. On the other hand, in Fig. 17(b), a second inflection point is clearly observed at $T_{Y1} = 262$ K and $T_{Y2} = 240$ K, in conventional and co-precipitate ferrites respectively. This behavior is attributed to a non-collinear arrangement of the magnetic moments in the A and B sites, i.e. it is due to a Yafet-Kittel-type ordering of the magnetic moments in both samples; the difference of temperatures ($T_{Y1} > T_{Y2}$) between both ferrites is indicative of an inhomogeneous distribution on occupancy of the B sites.

3.2.2. LFMA technique

In Fig. 18(a), we show LFMA spectra for conventional ferrite in the 208-408 K temperature range. This microwave absorption, around zero field, is far from the resonance condition given by eq.(3), i.e. the sample is in an unsaturated state; therefore, this absorption is associated with interaction between the microwave field and the dynamics of the magnetic domains structure in the sample. For $T > T_{c1}$ (= 408 K), LFMA spectra exhibit a linear behavior with a positive slope and non-hysteretic traces, and which is associate with paramagnetic phase, i.e. the long-range order has completely disappeared in the sample. For T_{YK1}(= 261 K) $\leq T \leq T_{c1}$, LFMA spectra show an antisymmetrical shape around zero field, displaying a clear hysteresis upon cycling the field, see Fig. 18(a); and they have the same phase of the EMR spectra, indicating that this absorption has a maximum value at zero field. For this temperature range, it can be observed that ΔH_{LFMA} increases when the temperature decreases, as can be seen in Fig. 18(b), for conventional and co-precipitate ferrites; this behavior indicates an increase in the ferromagnetically coupled superexchange interactions in the samples, suggesting that ΔH_{LFMA} is determined by the magnetic anisotropy and by the demagnetizing field (Montiel et al., 2004, 2005; Alvarez et al., 2008, 2010). But between both samples, the widths difference can be due to different distributions of cations in B sites, originating changes in the antiferromagnetic superexchange interactions; being more intense in the conventional Ni-Zn ferrite.

For $T < T_{YK1}$, an additional absorption mode also centered at zero field is observed in Fig. 18(a), and that it is suggested by high distortion of the LFMA signal at low temperature; this new absorption mode is more evident in co-precipitate ferrite (Alvarez et al., 2010). This signal exhibits an opposite phase (out-of-phase) with regard to EMR spectra; indicating that this microwave absorption has a minimum value at zero field. The presence of an out-of-phase signal has been correlated with the occurrence of a ferromagnetic order. It can be

assumed that a ferromagnetic arrangement is related with this signal, while a ferrimagnetic structure leads to the opposite result. Therefore, this out-of-phase signal can be associated with the appearance of a ferromagnetic arrangement of the magnetic moments in the sample; where a Yafet-Kittel-type canting of the magnetic moments in the B sites can provide this ferromagnetic component. Additionally, in this temperature region, ΔH_{LFMA} increases continuously with temperature decrease, but now with a higher change rate; this quick broaden is due to a build-up of the short-range magnetic correlations preceding to magnetic transition. For the above-mentioned, we propose that the phase transition at low temperature is due to a Yafet-Kittel-type magnetic ordering of the moments in the B sites, with onset at T_{YK1}; i.e. for $T<T_{YK1}$, the parallel arrangement of the B sites is modified, and a non-collinear arrangement of the magnetic moments in the A and B sites appears, leading to a change in the microwave absorption regime. It is necessary to mention that a similar behavior is observed in co-precipitate ferrite but with $T<T_{YK2}$ (= 239 K), see Fig. 18(b). The relevant temperatures are different but the dynamics of the magnetic moments is similar, detecting the Yafet-Kittel-type magnetic ordering around T_{YK2}, in a good correspondence with EMR technique. The difference of temperatures ($T_{YK1}>T_{YK2}$) between both ferrite is also indicative of a different occupancy of cations in the A and B sites.
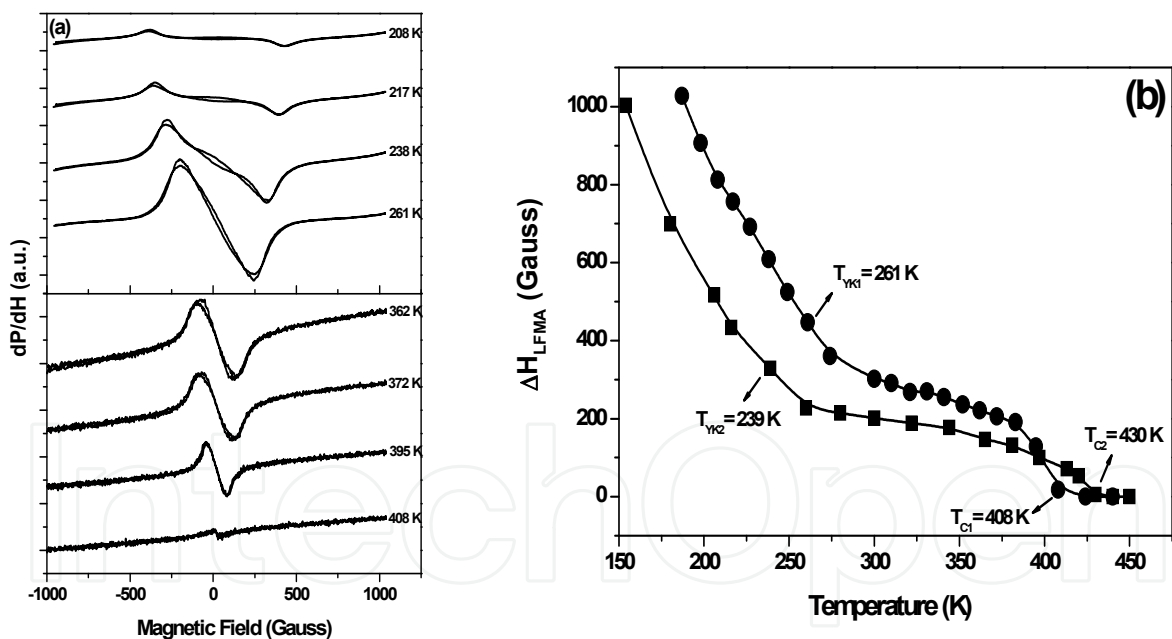

Figure 18. (a) LFMA spectra of the conventional Ni-Zn ferrite in the 362-408 K (down) and 208-261 K (up) temperature ranges. (b) Behavior of ΔH_{LFMA} for the (●) conventional and (■) co-precipitate Ni-Zn ferrites, as a function of temperature in the 150-450 K temperature range.

3.2.3. MAMMAS technique

We used MAMMAS technique to detect the ferri-paramagnetic transition in both ferrites sample. MAMMAS responses are shown in Fig. 19, where the measurements are carried out

heating and cooling the samples; with the purpose of looking a change associated with ferri-paramagnetic transition. For the sample of solid-state reaction, during heating (cooling), this signal increases monotonically as temperature increases (decreases) from 320 K (440 K), reaching a maximum value at T_{p1}=379 K (T^*_{p1}=355 K). As temperature increases (decreases) further, $T>T_{p1}$ ($T<T^*_{p1}$), the MAMMAS response decreases and another magnetic process sets-in, modifying its microwave absorption and this suggests a magnetic transition. An observed interesting feature in MAMMAS response is the absence of thermal hysteresis in the heating and cooling cycles, and it is only observed when $T \leq T_{H1}$(= 396 K); this merging point (T_{H1}) indicates the onset of the magnetic ordering. The T_{H1} value is in a very good agreement with the value of Curie temperature detected by the EMR and LFMA measurements. A similar MAMMAS response has been observed in co-precipitate ferrite in the 350-440 K temperature range, see the inset of the Fig. 19. The relevant temperatures are different but the dynamics of the magnetic moments is similar, detecting the ferri-paramagnetic transition around T_{H2}=424 K, in a good correspondence with EMR and LFMA techniques.
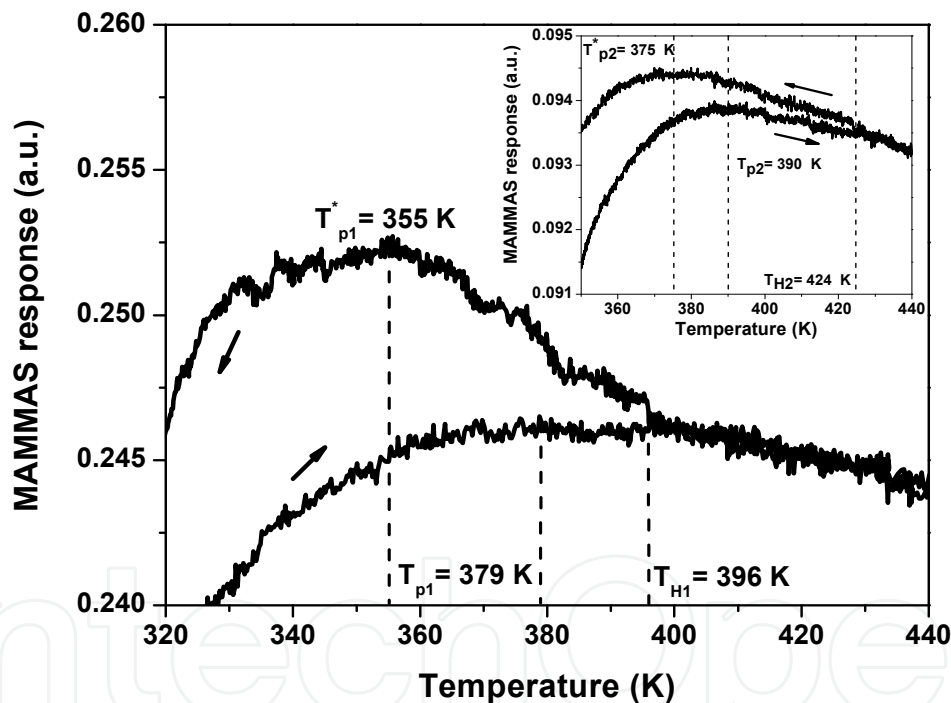

Figure 19. MAMMAS response of the conventional Ni-Zn ferrite in the 320-440 K temperature range; the inset shows the MAMMAS response of the co-precipitate Ni-Zn ferrite in the 350-440 K temperature range.

MAMMAS responses for these two ferrites, in 150-300 K temperature range, give us additional information on the magnetic transition at low temperature (see Fig. 20). Beginning to 300 K, these responses exhibit a continuous decrease to a minimum value at T_{m1}= 260 K and T_{m2}= 240 K, in conventional and co-precipitate ferrites respectively; and these absorptions increases when continuing diminishing the temperature. This feature points to a change in the microwave absorption regime due to a change in the magnetic structure

(Alvarez et al., 2010); revealing the appearance of a new population of absorbing centers, and which it also is suggested from EMR and LFMA measurements. All this profile shows that this change appears progressively as temperature is diminished, i.e. it is not a sharp change as could be expected from a structural phase transition. We associate this behavior with the transition from the collinear magnetic structure, $T>T_{m1}$ and $T>T_{m2}$, to the non-collinear (Yafet-Kittel-type) structure. Therefore, the MAMMAS responses depend on the thermal dependence of the magnetic moments dynamics, and the intensity of these signals follow the variations on the number of absorption centers (as is suggested by the EMR parameters), in turn is controlled by the establishment of the Yafet-Kittel-type canting of magnetic moments in the B sites at low temperature.
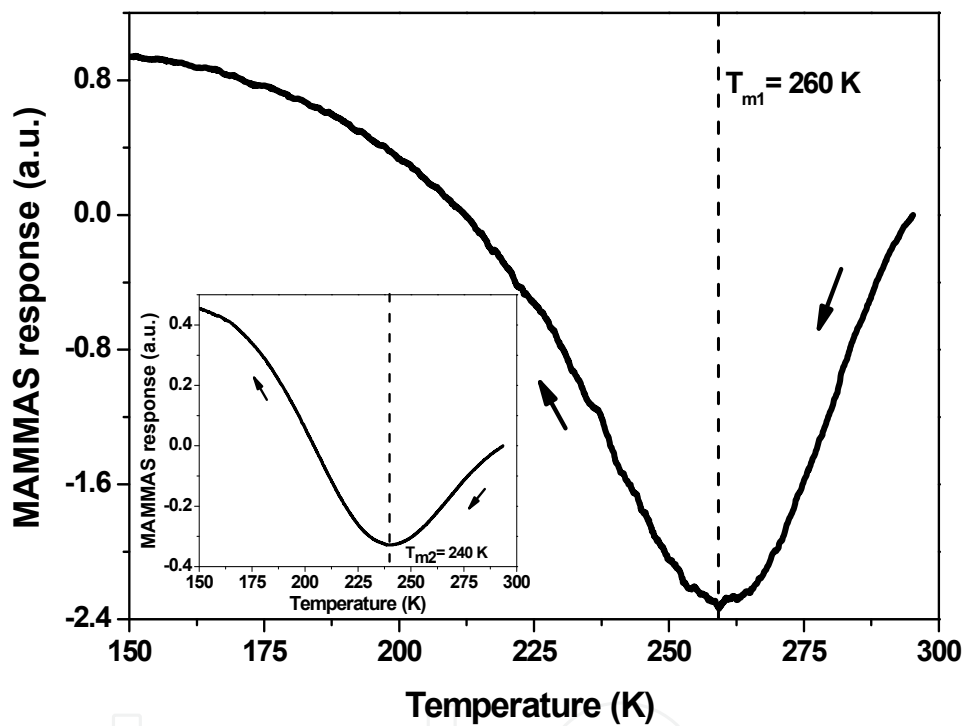

Figure 20. MAMMAS response of the conventional Ni-Zn ferrite in the 150-300 K temperature range; the inset shows the MAMMAS response of the co-precipitate Ni-Zn ferrite for same temperature range.

3.3. Néel transition (from a paramagnetic phase to antiferromagnetic ordering)

Lead iron tungstate, $Pb(Fe_{2/3}W_{1/3})O_3$ (PFW), shows an Néel transition around 350-380 K (Smolenskii et al., 1964; Feng et al., 2002; Ivanova et al., 2004); this magnetic ordering is due to superexchange interaction between the Fe ions through the O ions. For this study, PFW powders has been prepared through columbite precursor method (Zhou et al., 2000), where the purity of the powders was checked by means of XRD; all observed reflection lines are indexed as a cubic perovskite-type structure, in a good agreement with the standard data for PFW powders.

3.3.1. EMR technique

Fig. 21 shows the EMR spectra recorded in the 294-423 K temperature range. For 355 K $<T\leq$ 423 K, we observed a single broad Lorentzian line due to spin of the Fe^{+3} ions. In this lineshape kind, the derivative of the microwave power absorption with respect to the static field (dP/dH) can be fitted into two-component Lorentzian, accounting for the contributions from the clockwise and anticlockwise rotating components of the microwave magnetic field (Joshi et al., 2002). For $T \leq 355$ K, when the temperature goes diminishing, the absorption mode changes toward a broad asymmetric line of Dyson-type (Dyson, 1955; Feher & Kip, 1955) and their intensity diminishes; this Dyson lineshape is associated with a conductive contribution. This lineshape is a combination of an absorption component and other dispersion component of a symmetric Lorentzian mode, originating an additional parameter: the A/B ratio, i.e. the ratio of the amplitude of the left peak to that of the right peak of the EMR spectrum. Thus, EMR spectra are fitted to a functional form similar to the one used by Ivanshin et al. (2000). Additionally, for this temperature range, a second EMR mode (signal 2) is also observed; being more evident at room temperature, see Fig. 21.
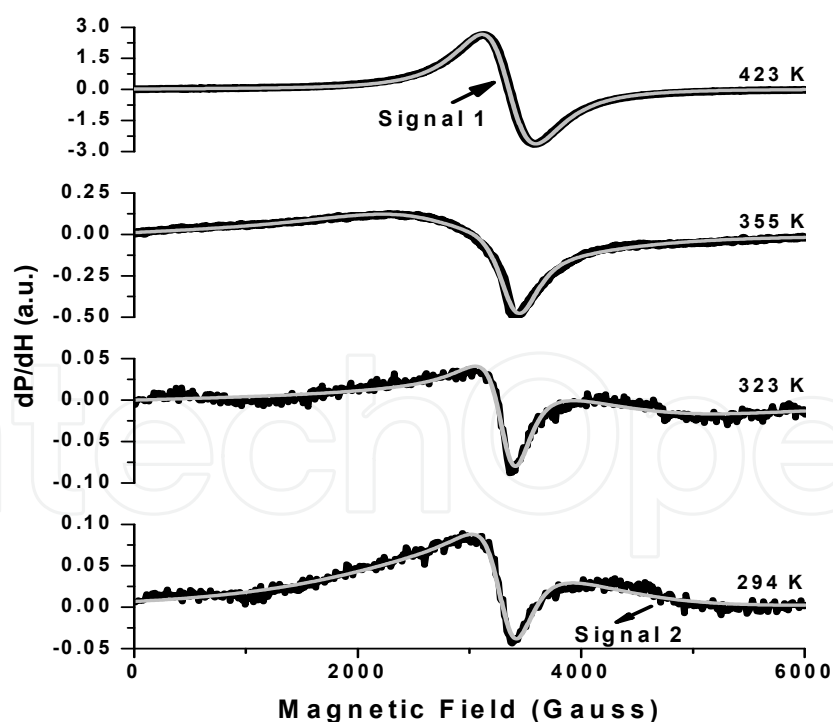

Figure 21. EMR spectra of PFW powders for selected temperatures; the solid lines correspond to the fits obtained from a functional form similar to the one used by Ivanshin et al. (2000).

In Fig. 22, the temperature dependences of the EPR parameters for signal 1 are plotted. ΔH_{PP} as a temperature function is shown in Fig. 22(a) for PFW powders. Starting from 423 K, as temperature decreases, ΔH_{PP} decreases continuously until 323 K; exhibiting a minimum at this temperature. This narrowing in ΔH_{PP} indicates an increase in the superexchange interactions in the sample, because the superexchange mechanism tend to narrow the absorption line; and it can be due to magnetic fluctuations, i.e. fluctuations in the establishment of the long-range order that precedes the transition to antiferromagnetic order. When continuing diminishing the temperature, T<323 K, ΔH_{PP} shows a weak increase until 294 K, this increase is indicative of a weak ferromagnetic behavior in the PFW; similar behaviors are observed in others magnetoelectric materials (Alvarez et al., 2006, 2010, 2012).

Fig. 22(b) shows the behavior of the g-factor vs. temperature for the signal 1, which is estimated from H_{res}, with $g= h\nu/\mu_B H_{res}$; where h is the Planck constant, ν is the frequency and μ_B is the Bohr magneton. EMR spectra give g-factor smaller than for a free electron (= 2.0023), along the entire temperature range. This behavior can be explained through the spin value of the Fe^{3+} ions (S=5/2) and to changes in the spin-orbit coupling; where the effective g-factor (g_{eff}) of a paramagnetic center is given by $g_{eff}=g(1\pm\kappa/\Delta)$, where Δ is the crystal-field splitting and κ is the spin-orbit coupling constant. The g-factor shows a weak decrease in the 423-365 K temperature range and then the g-factor continues diminishing, but this time with a higher change rate, reaching a minimum value at 344 K ($g_{min}= 1.8491$). This fast decrease can be due to build-up of magnetic correlations preceding the transition to the long-range antiferromagnetic ordering at Néel temperature ($T_N\sim$ 344 K). For T<T_N, the g-factor increases until 294 K and this behavior is an indication of a weak ferromagnetism in the PFW; this behavior can be due to a canting of the sublattices of Fe^{3+} ions in the antiferromagnetic matrix, generating an effective magnetic moment.

The temperature dependence of the A/B ratio is shown in Fig. 22(c). From this plot can be seen that, starting from 423 K to close to 378 K, the A/B ratio remains essentially constant at a value of 1. This value indicates that the paramagnetic centers are static and also suggests a strong dipolar interaction between Fe^{3+} ions. Further, the A/B ratio continually diminishes until a minimum value to 344 K; indicating a dispersion contribution and it suggests a conduction effect in the sample. As the temperature is decreased further, 294 K≤T<344 K, the A/B ratio increases toward a near value of 1, due to a decrease of the conductivity in sample. Recently, electric mensurations were carried out on PFW samples (Eiras et al. 2010; Fraygola et al. 2011), and which indicate a conductive contribution associated with an electronic-hoping mechanism, in a good correspondence with Dyson lineshape of the EMR spectra.

A second absorption mode (signal 2) is clearly observed at room temperature and it is associated with the presence of a fraction of Fe^{2+} ions, where oxygen atoms deficiency generate a state of mixed valency; originating a strong magnetic dipolar interaction between Fe^{2+} and Fe^{3+} ions, and that produces a broaden in absorption mode. In inset of the Fig. 22(a), we show the ΔH_{PP} behavior as a temperature function for the signal 2. For T<378 K, when diminishing the temperature, the broadening of signal 2 is indicative of an increase of the

interactions with Fe^{2+} ions. Additionally, a change in slope to 334 K is also observed; see the inset of the Fig. 22(a), where this feature can be associated with the para-antiferromagnetic transition.
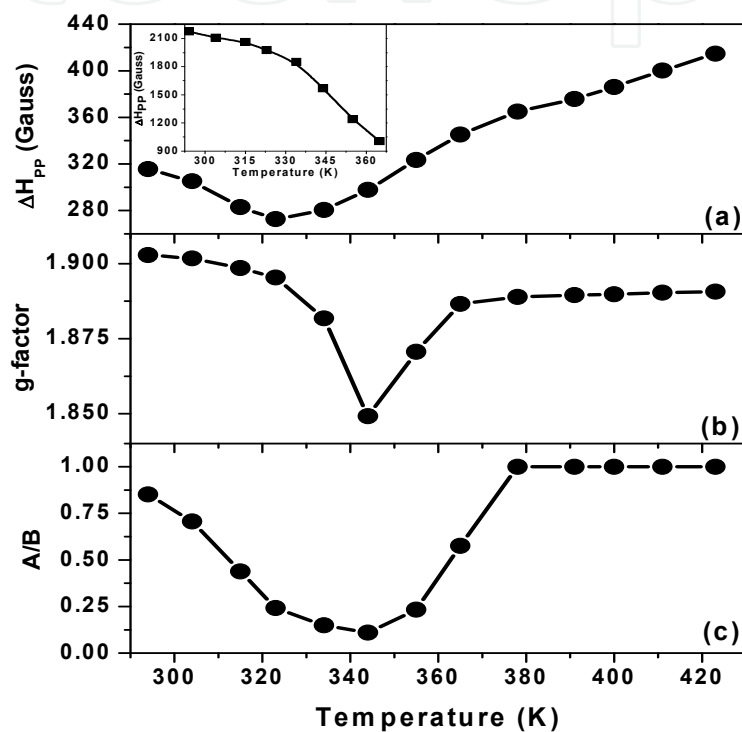

Figure 22. Temperature dependence of (a) ΔH_{PP}, (b) the g-factor and (c) the A/B ration of PFW powders for the signal 1; the inset of the Fig. 22(a) shows the temperature dependence of ΔH_{PP} for the signal 2. Solid lines are guides for the eye only.

3.3.2. LFMA technique

In Fig. 23(a), we show the LFMA signal in the 294-423 K temperature range. For all temperatures, LFMA signal exhibits two antisymmetric peaks about zero magnetic field, with opposed phase to EMR spectrum, and a clear hysteresis of this signal appears on cycling the field. This strongly contrasts with the LFMA signal observed in others

magnetoelectric materials (Alvarez et al., 2007, 2010, 2012), where these absorptions are lineal and non-hysteretic. The hysteresis feature has been associated with low field magnetization processes in ferromagnetic materials (Montiel et al., 2004; Alvarez et al., 2010; Gavi et al., 2012), suggesting the presence of a magnetic component in the material (Fraygola et al., 2011). With the help of a reference line, clearly one can observe that the LFMA signal has a lineal absorption component, see Fig. 23(a); where their slope is a temperature function. Fig. 23(b) shows the slope behavior of the lineal component for the 294-423 K temperature range. The slope increases monotonically when the temperature decreases from 423 K, reaching a maximum value at 365 K; this increasing behavior is characteristic of a paramagnetic phase. As the temperature is decreased further, T<365 K, the slope decreases very fast with decreasing temperature until T_{min}= 334 K; in this region the quantity of absorbing centers diminishes considerably due to the process of antiparallel spin alignment. Below T_{min}, the slope has an approximately lineal increase, where this behavior is a signature of the weak ferromagnetism in this temperature region (Alvarez et al., 2007, 2010, 2012).
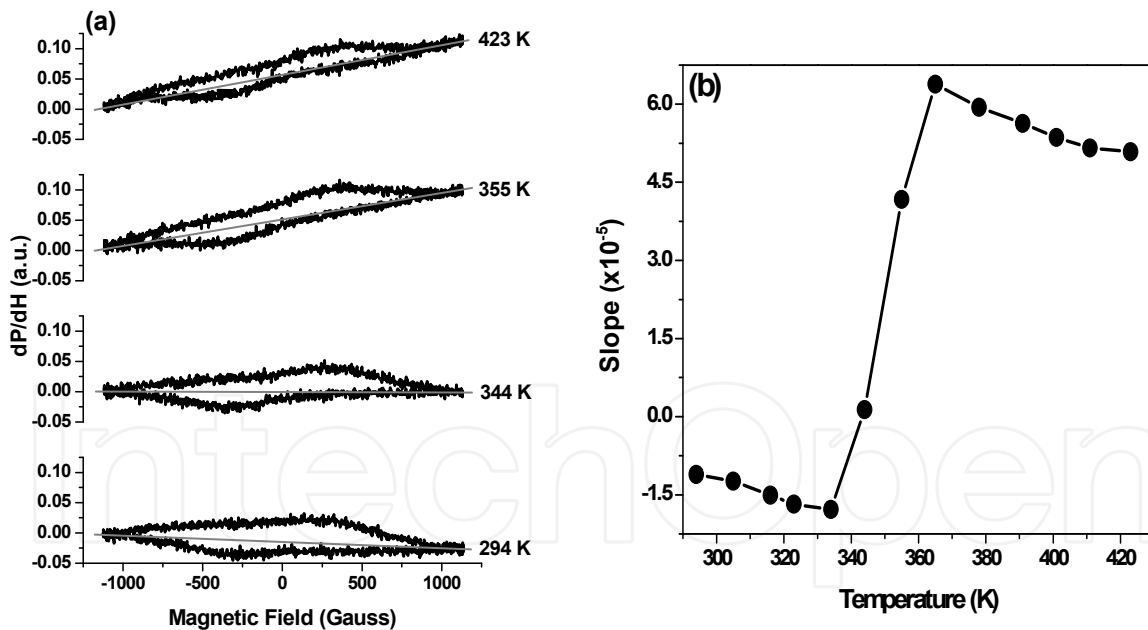

Figure 23. (a) LFMA signal for selected temperatures of PFW powders, where the straight lines are only a help to visualize the lineal component of the LFMA signal. (b) The slope temperature dependence of the lineal component for LFMA signal in the 294-423 K temperature range; the solid lines are guides for the eye only.

4. Conclusions

In this work is shown that EMR is the most powerful spectroscopic method available to determine the magnetic transitions in the materials. LFMA and MAMMAS techniques provide information on the dependences in temperature and magnetic field of the non-resonant microwave absorption. More important, these techniques can distinguish between different dissipative dynamics of microwave absorbing centers, providing valuable information about the nature of magnetic ordering within materials. We have shown that all these techniques are powerful tools for the research of magnetic materials at microwave frequencies.

Author details

H. Montiel
Centro de Ciencias Aplicadas y Desarrollo Tecnológico, Universidad Nacional Autónoma de México, Del. Coyoacán, México DF 04510, México

G. Alvarez
Escuela Superior de Física y Matemáticas del IPN, U.P.A.L.M, Edificio 9, San Pedro Zacatenco, México DF 07738, México

Acknowledgement

5. References

Akther Hossain A.K.M., Seki M., Kawai T., Tabata H., (2004) J. Appl. Phys. 96, 1273.

Alvarez G., Zamorano R., (2004) J. Alloys Compd. 369, 231.

Alvarez G., Font R., Portelles J., Valenzuela R., Zamorano R., (2006) Physica B 384, 322.

Alvarez G., Font R., Portelles J., Zamorano R., Valenzuela R., (2007) J. Phys. Chem. Solids 68, 1436.

Alvarez G., Montiel H., Cos D., García-Arribas A., Zamorano R., Barandiarán J.M., Valenzuela R., (2008) J. Non-Cryst. Solids 354, 5195.

Alvarez G., Font R., Portelles J., Raymond O., Zamorano R., (2009) Solid State Sci. 11, 881.

Alvarez G., Montiel H., Barron J.F., Gutierrez M.P., Zamorano R., (2010) J. Magn. Magn. Mater. 322, 348.

Alvarez, G., Cruz M.P., Durán A.C., Montiel H., Zamorano R., (2010) Solid State Commun. 150, 1597.

Alvarez G., Peña J.A., Castellanos M.A., Montiel H., Zamorano R., (2012) Rev. Mex. Fis. S 58(2), 24.

Andrzejewski B., Kowalczyk A., Stankowski J., Szlaferek A., (2004) J. Phys. Chem. Solids 65, 623.

Beach R.S., Berkowitz A. E., (1994) J. Appl. Phys. 76, 6209.

Bele P., Brunner H., Schweitzer D., J. Keller H., (1994) Solid State Commun. 92, 189.

Bhat S.V., Ganguly P., Ramakrishnan T.V., Rao C.N.R., (1987) J. Phys. C: Solid State Phys. 20, L559.

Bhide M.K., Kadam R.M., Sastry M.D., Ajay Singh, Shashwati Sen, Aswal D.K., Gupta S.K., Sahni V.C., (2001) Supercond. Sci. Technol. 14, 572.

Blazey K.W., Müller K.A., Bednorz J.G., Berlinger W., Amoretti G., Buluggiu E., Vera A., Matacotta F.C., (1987) Phys. Rev. B 36, 7241.

Bohandy J., Suter J., Kim B.F., Moorjani K., Adrian F.J., (1987) Appl. Phys. Lett. 51, 2161.

Byun T.Y., Byeon S.C., Hong K.S., Kyung C., (2000) J. Appl. Phys. 87, 6220.

Domínguez M., García-Beneytez J.M., Vázquez M., Lofland S.E., Baghat S.M., (2002) J. Magn. Magn. Mater. 249, 117.

Dyson F.J., (1955) Phys. Rev. 98, 349.

Eiras J.A., Fraygola B.M., Garcia D., (2010) Key Engineering Materials 434-435, 307.

Feher G., Kip A.F., (1955) Phys. Rev. 98, 337.

Feng L., Ye Z.G., (2002) J. Solid State Chem. 163, 484.

Fraygola B.M., Coelho A.A., Garcia D., Eiras J.A., (2011) Materials Research 14, 434.

Gavi H., Ngomb B.D., Beye A.C., Strydom A.M., Srinivasu V.V., Chaker M., Manyala N., (2012) J. Magn. Magn. Mater. 324, 1172.

Healy D.W., (1952) Phys. Rev. 86, 1009.

Hirotake Kajii, Hisashi Araki, Zakhidov A.A., Kazuya Tada, Kyuya Yakushi, Katsumi Yoshino, (1997) Physica C 277, 277.

Ivanova S.A., Eriksson S.G., Tellgrend R., Rundlöf H., (2004) Mater. Res. Bull. 39, 2317.

Ivanshin V.A., Deisenhofer J., Krug von Nidda H.-A., Loidl A., Mukhin A., Balbashov J., Eremin M.V., (2000) Phys. Rev. B 61, 6213.

Joshi J.P., Gupta R., Sood A.K., Bhat S.V., Raju A.R., Rao C.N.R., (2002) Phys. Rev. B 65, 024410.

Khachaturyan K., Weber E.R., Tejedor P., Stacy A.M., Portis A.M., (1987) Phys. Rev. B 36, 8309.

Kheifets A.S., Veinger A.I., (1990) Physica C 165, 491.

Kim B.F., Moorjani K., Adrian F.J., Bohandy J., (1993) Materials Science Forum 137-139, 133.

Montiel H., Alvarez G., Gutierrez M.P., Zamorano R., Valenzuela R., (2004) J. Alloys Compd. 369, 141.

Montiel H., Alvarez G., Betancourt I., Zamorano R., Valenzuela R., (2005) Appl. Phys. Lett. 86, 072503.

Montiel H., Alvarez G., Betancourt I., Zamorano R., Valenzuela R., (2006) Physica B 384, 297.

Montiel H., Alvarez G., Zamorano R., Valenzuela R., (2007) J. Non-Cryst. Solids 353, 908.

Montiel H., Alvarez G., Zamorano R., Valenzuela R., (2008) J. Non-Cryst. Solids 354, 5192.

Moorjani K., Bohandy J., Adrian F.J., Kim B.F., (1987) Phys. Rev. B 36, 4036.

Nabereznykh V.P., Tsindlekht M.I., (1982) JETP Lett. 36, 157.

Niebling U., Steinl J., Schweitzer D., Strunz W., (1998) Solid State Commun. 106, 505.

Okamura T., Torizuka Y., Kojima Y., (1951) Phys. Rev. 82, 285.

Okamura T., (1951) Nature 168, 162.

Owens F.J., (1997) J. Phys. Chem. Solids 58, 1311.

Owens F.J., (2001) Physica C 363, 202.

Pacher N., Deisenhofer J., Krung von Nidda H.-A., Hemmida M., Jeevan H.S., Gegenwart P., Loidl A., (2010) Phys. Rev. B 82, 054525.

Padam G.K., Ekbote S.N., Tripathy M.R., Srivastava G.P., Das B.K., (1999) Physica C 315, 45.

Padam G.K., Arora N.K., Ekbote S.N., (2010) Mater. Chem. Phys. 123, 752.

Panarina N.Y., Talanov Y.I., Shaposhnikova T.S., Beysengulov N.R., Vavilona E., Behr G., Kondrat A., Hess C., Leps N., Wurmehl S., Klinger R., Kataev V., Büchner B., (2010) Phys. Rev. B 81, 224509.

Pong W.F., Chang Y.K., Su M.H., Tseng P.K., Lin H.J., Ho G.H., Tsang K.L., Chen C.T., (1997) Phys. Rev. B 55, 11409.

Priyadharsini P., Pradeep A., Sambasiva Rao P., Chandrasekaran G., (2009) Mater. Chem. Phys. 116, 207.

Ravindaranathan P., Patil K.C., (1987) J. Mater. Sci. 22, 3261.

Satya Murthy N.S., Natera M.G., Youssef S.I., Begum R.J., Srivastava C.M., (1969) Phys. Rev. 181, 969.

Schlomann E., (1958) J. Phys. Chem. Solids 6, 257.

Shaltiel D., Bezalel M., Revaz B., Walker E., Tamegai T., Ooi S., (2001) Physica C 349, 139.

Smolenskii G.A., Bokov V.A., (1964) J. Appl. Phys. 35, 915.

Srivastava C.M., Patni M.J., (1974) J. Magn. Res. 15, 359.

Stankowski J., Piekara-Sady L., Kempinski W., (2004) J. Phys. Chem. Solids 65, 321.

Topacli C., (1996) J. Supercond. 9, 263.

Topacli C., (1998) Physica C 301, 92.

Velter-Stefanescu M., Totovana A., Sandu V., (1998) J. Supercond. 11, 327.

Velter-Stefanescu M., Duliu O.G., Mihalache V., (2005) J. Optoelectron. Adv. M. 7, 1557.

Wu K.H., Shin Y.M., Yang C.C., Wang G.P., Horng D.N., (2006) Mater. Lett. 60, 2707.

Yafet Y., Kittel C., (1952) Phys. Rev. 87, 290.

Yildiz F., Rameev B.Z., Tarapov S.I., Tagirov L.R., Aktas B., (2002) J. Magn. Magn. Mater. 247, 222.

Zakhidov A.A., Ugawa A., Imaeda K., Yakushi K., Inokuchi H., (1991) Solid State Commun. 79, 939.

Zhou L., Vilarinho P.M., Bptista J.L., Fortunato E., (2000) J. Eur. Ceram. Soc. 20, 1035.